Article:

eprints@whiterose.ac.uk
https://eprints.whiterose.ac.uk/

Mapping Circumstellar Matter with Polarized Light: The Case of Supernova 2014J in M82

Yi Yang (杨轶)[1,2] , Lifan Wang[1,3], Dietrich Baade[4], Peter. J. Brown[1] , Aleksandar Cikota[4] , Misty Cracraft[5] ,
Peter A. Höflich[6], Justyn R. Maund[7,10] , Ferdinando Patat[4] , William B. Sparks[5] , Jason Spyromilio[4] ,
Heloise F. Stevance[7] , Xiaofeng Wang[8] , and J. Craig Wheeler[9]

[1] George P. and Cynthia Woods Mitchell Institute for Fundamental Physics & Astronomy, Texas A. & M. University, Department of Physics and Astronomy, 4242 TAMU, College Station, TX 77843, USA; yi.yang@weizmann.ac.il
[2] Department of Particle Physics and Astrophysics, Weizmann Institute of Science, Rehovot 76100, Israel
[3] Purple Mountain Observatory, Chinese Academy of Sciences, Nanjing 210008, People's Republic of China
[4] European Organisation for Astronomical Research in the Southern Hemisphere (ESO), Karl-Schwarzschild-Str. 2, D-85748 Garching b. München, Germany
[5] Space Telescope Science Institute, Baltimore, MD 21218, USA
[6] Department of Physics, Florida State University, Tallahassee, Florida 32306-4350, USA
[7] Department of Physics and Astronomy, University of Sheffield, Hicks Building, Hounsfield Road, Sheffield S3 7RH, UK
[8] Physics Department and Tsinghua Center for Astrophysics (THCA), Tsinghua University, Beijing, 100084, People's Republic of China
[9] Department of Astronomy and McDonald Observatory, The University of Texas at Austin, Austin, TX 78712, USA

Abstract

Optical polarimetry is an effective way of probing the environment of a supernova for dust. We acquired linear *HST* ACS/WFC polarimetry in bands $F475W$, $F606W$, and $F775W$ of the supernova (SN) 2014J in M82 at six epochs from ∼277 days to ∼1181 days after the B-band maximum. The polarization measured at day 277 shows conspicuous deviations from other epochs. These differences can be attributed to at least ∼$10^{-6} M_{\odot}$ of circumstellar dust located at a distance of ∼5×10^{17} cm from the SN. The scattering dust grains revealed by these observations seem to be aligned with the dust in the interstellar medium that is responsible for the large reddening toward the supernova. The presence of this circumstellar dust sets strong constraints on the progenitor system that led to the explosion of SN 2014J; however, it cannot discriminate between single- and double-degenerate models.

Key words: circumstellar matter – dust, extinction – polarization – supernovae: individual (SN 2014J)

1. Introduction

The explosions of type Ia supernovae (SNe) are powered by the thermonuclear runaway of (∼$1M_{\odot}$) carbon/oxygen white dwarfs (C/O WDs; Hoyle & Fowler 1960). The homogeneity of type Ia SNe lightcurves (i.e., Barbon et al. 1973; Elias et al. 1981) and the correlation between the decline rate of the light curve and the luminosity at peak (Phillips 1993) enable the usage of type Ia SNe as the most accurate distance indicators at redshifts (z) out to ∼2 (Riess et al. 1998; Perlmutter et al. 1999; Riess et al. 2016). The exact progenitor systems of type Ia SN explosions remain unknown.

Some evidence suggests a non-degenerate companion scenario in which a compact WD accretes matters from a subgiant or a main sequence star. Examples include the time evolution of Na D_2 features after the B-band maximum light of SN 2006X (Patat et al. 2007), an excess of blue light from a normal type Ia SN 2012cg at 15 and 16 days before the B-band maximum light (Marion et al. 2016), and a UV flash within about five days after the explosion of iPTF14atg (Cao et al. 2015), although iPTF14atg is about three magnitudes subluminous compared to a normal type Ia SN. Very recently, high-cadence photometric observation of the type Ia SN 2017cbv has revealed a blue excess during the first ∼1–5 days after the explosion (Hosseinzadeh et al. 2017). Although the blue bump in the light curve can be explained by the SN ejecta interacting with a subgiant star, it could also be due to interaction with CSM or the presence of nickel in the outer ejecta (Hosseinzadeh et al. 2017).

Other observations favor a double degenerate scenario featuring the merger of two WDs (Iben & Tutukov 1984; Webbink 1984), see, for example, SN 2011fe (Nugent et al. 2011; Bloom et al. 2012). Observations also excluded any luminous red giant companion (see, for example, Li et al. 2011), but the missing companions could also be M dwarfs (Wheeler 2012). For the first few days after the explosion, a collision between material ejected by the SN and a non-degenerate companion star would produce optical/UV emission in excess of the rising luminosity from radioactive decay (Kasen 2010). In particular, monitoring of three photometrically normal type Ia SNe with the *Kepler* satellite during their entire rising phase (Olling et al. 2015) shows no evidence of interaction between SN ejecta and circumstellar matter (CSM) or companion stars, thus ruling out the possibility of red giants or larger companions predicted by single degenerate models. The absence of CSM around type Ia SNe supports double degenerate progenitor models; however, searches for CSM around type Ia SNe are difficult, and the results have been in most cases inconclusive. Deep *HST* imaging of type Ia SN remnant SNR 0509−67.5 in the Large Magellanic Cloud found no signs of a surviving ex-companion star. Searches for surviving companions of the progenitor have excluded all giant and subgiant companions for SN 1006 (González Hernández et al. 2012; Kerzendorf et al. 2017), and companions with $L > 10 L_{\odot}$ for SN 1604 (*Kepler* supernova, Kerzendorf et al. 2014). These results strongly disfavor the single-degenerate models (Schaefer & Pagnotta 2012). However, see a possible exception for SN 1572 in Ruiz-Lapuente et al. (2004).

---

[10] Royal Society Research Fellow.

The merger of two compact stars is a very asymmetric process, which should lead to a strong polarimetric signature (Bulla et al. 2016). By contrast, observations consistently find a lack of intrinsic polarization before optical maximum (Wang et al. 2008; Maund et al. 2013), which seems to cast doubt on the double degenerate models (Wang et al. 2008; Rimoldi et al. 2016). Quantifying the amount of CSM is of high importance for the understanding of the progenitor systems of type Ia SNe.

Moreover, better estimation of interstellar extinction reduces systematic uncertainties. Characterization of dust in the diffuse interstellar medium (ISM) relies heavily on the observed wavelength dependence of extinction and polarization (Voshchinnikov et al. 2012; Patat et al. 2015). The observed wavelength dependence of interstellar extinction R_V contains information on both the size and composition of the grains. The value of $R_V = 3.1$ (Cardelli et al. 1989) has often been considered the Galactic standard, but with a range from 2.2 to 5.8 (Fitzpatrick 1999) for different lines of sight. There is increasing evidence that extinction curves toward type Ia SNe systematically favor a steeper law ($R_V < 3$; see, e.g., Nobili & Goobar (2008), and Cikota et al. (2016) for a summary of R_V results of earlier studies). This discrepancy has remained unexplained. It is very important to understand whether systematically low R_V values toward type Ia SNe are caused by systematic differences between the dust compositions of the host galaxies.

Wang (2005) and Patat et al. (2006) have proposed that circumstellar dust scattering may be a solution to the surprisingly low R_V values toward type Ia SNe, due to a time-dependent scattering process. Goobar (2008) confirmed these results without including the time-dependent radiative transfer effect. The effect on R_V and the light curve shape, however, also depends on the large-scale geometrical configuration and the properties of the dust grains (Amanullah & Goobar 2011; Brown et al. 2015). For example, recent observations of the highly reddened SN 2014J in M82 have found no convincing evidence of the presence of circumstellar dust (Brown et al. 2015; Patat et al. 2015; Johansson et al. 2017; Kundu et al. 2017; Bulla et al. 2018; see, however, Foley et al. 2014; Hoang 2017).

Observations in polarized light and its time evolution can be an effective way of studying the CSM. Type Ia SNe have low intrinsic polarization in broadband observations ($\lesssim 0.2\%$, Wang et al. 2008), whereas the scattered light from CSM can be highly polarized. The maximal degree of linear polarization (p_{max}) of light scattered by dust can reach $\sim 50\%$ in the V-band, as reported by, e.g., Sparks et al. (2008) for the light echo from the dusty nebula around the eruptive star V838 Mon and by Kervella et al. (2014) for the nebula that contains the δ Cepheid RS Pup). More typical values of p_{max} in the Milky Way are 20%–30% (Draine 2003). Theoretical models (Mathis & Whiffen 1989) suggest that interstellar dust grains are loose structures with high porosity. This is confirmed by probes of cometary dust collected by space and ground-based missions (e.g., Noguchi et al. 2015; Schulz et al. 2015), which, according to Greenberg (1986), is a proxy of ISM dust. Polarimetry of cometary dust found p_{max} values of 10%–30% (e.g., see Figure 1 of Petrova et al. 2000 and a review by Mann et al. 2006), comparable to the values in the Milky Way ISM. In laboratory experiments with analog fluffy aggregates, polarizations in the 50%–100% range were measured (Volten et al. 2007). In a very recent study, Sen et al. (2017) concluded that, over the range in porosity of 0%–50%, p_{max} varies

nonmonotonically and can reach or exceed 60%. For a spatially unresolved source, the scattered light can contribute significantly to the total integrated light and associated distance estimates. In addition, polarization of the integrated light can evolve rapidly after maximum light (Wang & Wheeler 1996). The fraction of polarized flux from any nonaxisymmetric circumstellar dust increases substantially as the SN dims and scattered photons (often from light at optical maximum) contribute significantly to the SN light curve at late phases. The actual situation may be more complicated, as the dust distribution can be more uniform around the SN than the often assumed single clump, and the effect on the polarization and the light curve may be less dramatic. In general, the effect is qualitatively stronger in the blue than in the red, due to the higher scattering opacity in the blue.

SN 2014J was discovered on January 21.805 UT (Fossey et al. 2014; Ma et al. 2014), and the first light has been constrained to be January 14.75 UT (Zheng et al. 2014; Goobar et al. 2015). SN 2014J reached its B-band maximum on February 2.0 UT (JD 2,456,690.5) at a magnitude of 11.85 ± 0.02 (Foley et al. 2014). Exploding in the nearby starburst galaxy M82 at a distance of 3.53 ± 0.04 Mpc (Dalcanton et al. 2009), SN 2014J was the nearest SN since SN 1987A. The relative proximity of SN 2014J allows continuous photometric and spectroscopic observations through late phases (Lundqvist et al. 2015; Bonanos & Boumis 2016; Porter et al. 2016; Sand et al. 2016; Srivastav et al. 2016; Johansson et al. 2017; Yang et al. 2018). SN 2014J suffers from heavy extinction and is located behind a large amount of interstellar dust (Amanullah et al. 2014). There is ample evidence that the strong extinction is caused primarily by interstellar dust (Brown et al. 2015; Patat et al. 2015; Bulla et al. 2018); however, high-resolution spectroscopy does show strong evidence of time-evolving K I lines that can be understood as due to photo-ionization of material located at a distance of about 10^{19} cm from the SN (Graham et al. 2015). Moreover, numerous Na, Ca, and K features along the SN-Earth line of sight were detected (Patat et al. 2015). No positive detection of any material at distances within 10^{19} cm has been reported for SN 2014J, but see Foley et al. (2014), Brown et al. (2015), and Bulla et al. (2016) for an alternate view. In this paper, we present our late-time HST imaging polarimetry of SN 2014J and derive from it the amount of circumstellar dust around SN 2014J.

2. Observations and Data Reduction

The HST WFC/ACS camera has a polarimetry mode that allows for accurate imaging polarimetry. The filter-polarizer combinations that we selected have been calibrated recently (Avila 2017). We used the Advanced Camera for Surveys/Wide Field Channel (ACS/WFC) onboard the HST to observe SN 2014J in imaging polarization mode at six epochs (V1-V6) under multiple HST programs: GO-13717 (PI: Wang), GO-14139 (PI: Wang), and GO-14663 (PI: Wang). The observations were taken with three different filters, $F475W$ ($SDSSg$), $F606W$ (broad$V$), and $F775W$ ($SDSSi$), each combined with one of the three polarizing filters, POL0V, POL60V, and POL120V, oriented at relative position angles (PA) of 0°, 60°, and 120°, respectively. A log of observations is presented in Table 1. Multiple dithered exposures were taken at each observing configuration to allow for drizzling of the images. Exposure

Table 1
Log of Observations of SN 2014J with *HST* ACS/WFC POL * V

Filter	Polarizer	Date (UT)	Exp (s)	Phase[a] (Days)	Date (UT)	Exp (s)	Phase[a] (Days)	Date (UT)	Exp (s)	Phase[a] (Days)
F475W	POL0V	2014 Nov 06	3 × 130	276.5	2015 Mar 25	3 × 400	415.6	2015 Nov 12	4 × 1040	648.5
F475W	POL120V	2014 Nov 06	3 × 130	276.5	2015 Mar 25	3 × 400	415.6	2015 Nov 12	4 × 1040	648.7
F475W	POL60V	2014 Nov 06	3 × 130	276.5	2015 Mar 25	3 × 400	415.7	2015 Nov 12	4 × 1040	648.8
F606W	POL0V	2014 Nov 06	2 × 40	276.6	2015 Mar 27	3 × 60	417.9	2015 Nov 12	4 × 311	649.0
F606W	POL120V	2014 Nov 06	2 × 40	276.6	2015 Mar 27	3 × 60	418.0	2015 Nov 13	4 × 311	649.0
F606W	POL60V	2014 Nov 06	2 × 40	276.6	2015 Mar 27	3 × 60	418.0	2015 Nov 13	4 × 311	649.1
F775W	POL0V	2014 Nov 06	2 × 30	276.6	2015 Mar 27	3 × 20	418.0	2015 Nov 12	4 × 100	648.5
F775W	POL120V	2014 Nov 06	1 × 55	276.6	2015 Mar 27	3 × 20	418.0	2015 Nov 12	4 × 100	648.7
F775W	POL60V	2014 Nov 06	1 × 55	276.6	2015 Mar 27	3 × 20	418.0	2015 Nov 12	4 × 100	648.9
F475W	POL0V	2016 Apr 08	4 × 1040	796.2	2016 Oct 12	4 × 1040	983.1	2017 Apr 28	4 × 1040	1181.3
F475W	POL120V	2016 Apr 08	4 × 1040	796.4	2016 Oct 12	4 × 1040	983.3	2017 Apr 28	4 × 1040	1181.4
F475W	POL60V	2016 Apr 08	4 × 1040	796.6	2016 Oct 12	4 × 1040	983.4	2017 Apr 28	4 × 1040	1181.5
F606W	POL0V	2016 Apr 08	4 × 311	796.8	2016 Oct 14	3 × 360	985.1	2017 Apr 28	3 × 360	1181.7
F606W	POL120V	2016 Apr 08	4 × 311	796.8	2016 Oct 14	3 × 360	985.1	2017 Apr 28	3 × 360	1181.7
F606W	POL60V	2016 Apr 08	4 × 311	796.9	2016 Oct 14	3 × 360	985.1	2017 Apr 28	3 × 360	1181.7
F775W	POL0V	2016 Apr 08	4 × 100	796.2	2016 Oct 12	4 × 202	983.1	2017 Apr 28	4 × 202	1181.3
F775W	POL120V	2016 Apr 08	4 × 100	796.4	2016 Oct 12	4 × 202	983.3	2017 Apr 28	4 × 202	1181.4
F775W	POL60V	2016 Apr 08	4 × 100	796.6	2016 Oct 12	4 × 202	983.4	2017 Apr 28	4 × 202	1181.5

Note.
[a] Days since B maximum on 2014 February 2.0 (JD 245 6690.5).

times ranged from 30 s with *F775W* on day 276–1040 s with *F475W* on day 1181.

The *HST* data were reduced following the usual routine of drizzling to remove artifacts and cosmic rays. For each bandpass and polarizer, one combined image was prepared. Bright HII regions in the field-of-view (FOV) were used to align exposures in different bandpass+polarizer combinations and epochs through *Tweakreg* in the *Astrodrizzle* package (Gonzaga et al. 2012). The polarizers contain a weak optical lens that corrects the optical focus for the presence of bandpass +polarizer filters in the light path. Large-scale distortions introduced by this weak optical lens have been removed using the *Astrodrizzle* software. All images were aligned to better than 0.25 pixels in both *x* and *y* directions. This is compatible with the small-scale distortion (±0.3 pixel) in the images caused by slight ripples in the polarizing material (see the ACS Data Handbook; Lucas et al. 2016).

The absolute throughput values of bandpass+polarizer combinations listed in the *Synphot*[11] software does not match those found in on-orbit calibrations. Correction factors by Cracraft & Sparks (2007) based on on-orbit calibration programs were used to remove the instrumental polarization. The scaling factors (C_{POL*V}) have been applied to images obtained with each polarizer: $r(POL * V) = C_{POL*V} * Im(obs)_{POL*V}$. The remaining instrumental polarization can still be as much as ∼1%, and the instrumental polarization has been observed to vary with roll angle (e.g., see Cracraft & Sparks 2007 and Lucas et al. 2016). To improve the measurement precision, we use bright sources in the field (for visits V1 and V2) to monitor the stability of the instrumental polarization. The roll angles in the subsequent observing epochs were set to be either equal to or 180° different from the roll angles in V1 and V2. We discuss this further in Section 3.

2.1. Measuring the Degree of Polarization

We deduced the Stokes (*I*, *Q*, *U*) from the observations as follows:

$$I = \frac{2}{3}[r(POL0) + r(POL60) + r(POL120)],$$
$$Q = \frac{2}{3}[2r(POL0) - r(POL60) - r(POL120)],$$
$$U = \frac{2}{\sqrt{3}}[r(POL60) - r(POL120)], \quad (1)$$

where *I*, *Q*, and *U* are standard notation of the components of the Stokes vector. Flux measurements were made with a circular aperture of 0.″15 (three pixels in the ACS/WFC FOV) to reduce the contamination from the extremely non-uniform background. Aperture corrections were calculated with the ACS/WFC encircled energy profile for each bandpass, according to Sirianni et al. (2005). We perform the measurements of the SN on the images obtained by each polarizer $r(POL * V)$. We also deduce the Stokes *I*, *Q*, *U* maps using Equation (1), integrating within the aperture centered at the SN on the Stokes *I*, *Q*, *U* maps. In both cases, the background has been estimated by choosing the same inner and outer radii as used by Yang et al. (2018). The two approaches agree within the uncertainties when the signal-to-noise (S/N) ratio on each $r(POL * V)$ is S/N > 50. Figure 1 presents a color composite image of SN 2014J consisting of the Stokes *I* data for each bandpass and epoch. The images show resolved light echoes expanding over time, which were first identified by Crotts (2015). We only remark here that these multiple light echoes are produced by dust clouds at a distance about 100–500 pc away from SN 2014J. The dust in those sheets is unlikely to be related to the evolution of the SN progenitor. Detailed studies of these resolved light echoes were performed on the same *HST* data as those used for the present study, and can be found in Yang et al. (2017).
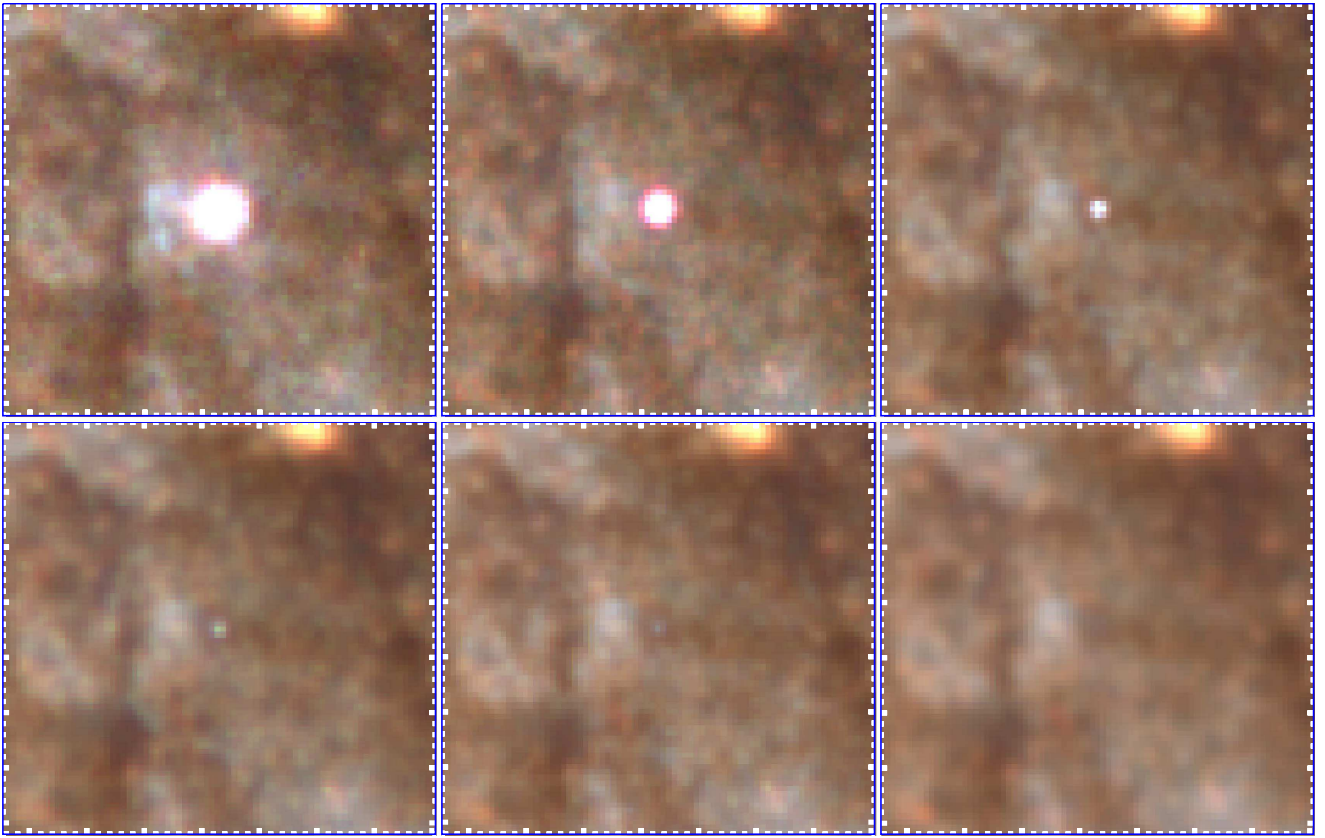
Figure 1. Color images of SN 2014J from *HST* ACS/WFC *F475W*, *F606W*, and *F775W* observations on days 277 (upper left), 416 (upper middle), 649 (upper right), 796 (lower left), 985 (lower middle), and 1181 (lower right) after maximum light. North is up, east is left, and the distance between big tick marks corresponds to $0\rlap{.}''5$ or 8.6 pc projected on the plane of the sky. Reflection of SN light by the dust between the SN and the observer creates arcs of light echoes that propagate with time. There may also be unresolved light echoes at distances so close to the central SN that even the *HST* cannot resolve them, but imaging polarimetry can still detect their presence.

The degree of polarization and the polarization PA can be derived as:

$$p\% = \frac{\sqrt{Q^2 + U^2}}{I} \times \frac{T_{\mathrm{par}} + T_{\mathrm{perp}}}{T_{\mathrm{par}} - T_{\mathrm{perp}}} \times 100\%, \qquad (2)$$

$$\mathrm{PA} = \frac{1}{2}\tan^{-1}\left(\frac{U}{Q}\right) + \mathrm{PA\_V3} + \chi. \qquad (3)$$

The SN fluxes measured in the different "bandpass+polarizer" combinations were then converted to polarization measurements following the *HST* ACS manual (Avila 2017) and earlier work (Sparks & Axon 1999). The cross-polarization leakage is insignificant for visual polarizers (Biretta et al. 2004). The factor containing the parallel and perpendicular transmission coefficients $(T_{\mathrm{par}} + T_{\mathrm{perp}})/(T_{\mathrm{par}} - T_{\mathrm{perp}})$ is about unity and has been corrected in our data reduction. The degree of polarization ($p\%$) is calculated using the Stokes vectors. These corrections, together with the calibration of the source count rates, vectorially remove the instrumental polarization of the WFC ($\sim1\%$). The polarization PA is calculated using the Stokes vectors and the roll angle of the *HST* spacecraft (PA_V3 in the data headers), as shown in Equation (3). Another parameter, called χ, containing information about the camera geometry derived from the design specification, has been considered when solving the matrix to deduce the Stokes vectors. For the WFC, $\chi = -38\rlap{.}°2$ (Lucas et al. 2016).

2.2. Errors in Polarimetry

The classical method proposed by Serkowski (1958, 1962) is often used for the determination of the polarization and associated uncertainties. Montier et al. (2015) investigated the statistical behavior of basic polarization fraction and angle measurements. We use Equations (4) and (5) to describe the uncertainty of p and PA, where σ_I, σ_Q, σ_U denotes the associated errors in individual measurement of the Stokes I, Q, U; σ_{QU}, σ_{IQ}, σ_{IU} denotes the covariance between the associate Stokes parameters. The detailed derivation is available in Appendix F of Montier et al. (2015).

$$\sigma_p^2 = \frac{1}{p^2 I^4} \times (Q^2\sigma_Q^2 + U^2\sigma_U^2 + p^4 I^2\sigma_I^2$$
$$+ 2QU\sigma_{QU} - 2IQp^2\sigma_{IQ} - 2IUp^2\sigma_{IU}), \qquad (4)$$

$$\sigma_{\mathrm{P.A}} = \sqrt{\frac{Q^2\sigma_U^2 + U^2\sigma_Q^2 - 2QU\sigma_{QU}}{Q^2\sigma_Q^2 + U^2\sigma_U^2 + 2QU\sigma_{QU}}} \times \frac{\sigma_p}{2p} \ \mathrm{rad}. \qquad (5)$$

The Stokes I component gives the total intensity of the source. The AB magnitudes of the SN were obtained by applying the ACS/WFC zeropoints.

The degree of polarization and the magnitudes of the SN in different filter bands are shown in Table 2. The other sources of data used in this paper include three epochs of observations (Patat et al. 2015) using the polarimetric mode of the Calar Alto Faint Object Spectrograph (CAFOS, see Patat & Taubenberger 2011)

Table 2
The Polarization Degree of SN 2014J

Filter	Phase Days	p %	PA degrees	mag	Phase Days	p %	PA degrees	mag
F475W	276.5	3.82 ± 0.12	40.3 ± 0.9	17.363 ± 0.001	415.6	4.56 ± 0.21	37.7 ± 1.2	19.464 ± 0.002
F606W	276.6	2.65 ± 0.21	46.9 ± 2.3	17.429 ± 0.002	417.9	3.27 ± 0.48	43.4 ± 3.5	19.594 ± 0.003
F775W	276.6	1.19 ± 0.24	41.7 ± 7.5	16.742 ± 0.002	418.0	1.55 ± 0.58	17.1 ± 6.2	18.268 ± 0.004
F475W	648.5	4.68 ± 0.44	33.3 ± 2.6	22.363 ± 0.003	796.2	3.50 ± 0.81	33.0 ± 6.6	23.266 ± 0.006
F606W	649.0	4.57 ± 0.58	47.7 ± 3.7	21.962 ± 0.005	796.8	0.78 ± 1.19	73.2 ± 43.6	22.917 ± 0.009
F775W	648.5	4.49 ± 0.75	39.9 ± 4.8	21.427 ± 0.006	796.2	2.40 ± 1.48	54.1 ± 17.5	22.492 ± 0.011
F475W	983.1	2.27 ± 1.84	48.3 ± 23.6	24.169 ± 0.014	1181.4	5.61 ± 2.76	59.2 ± 16.0	24.765 ± 0.023
F606W	985.1	6.58 ± 3.09	53.5 ± 13.9	23.934 ± 0.024	1181.7	3.12 ± 5.88	37.4 ± 53.2	24.695 ± 0.049
F775W	983.1	8.43 ± 1.99	68.3 ± 6.8	23.294 ± 0.015	1181.4	7.61 ± 4.19	104.6 ± 15.5	24.234 ± 0.032

instrument at the 2.2 m telescope in Calar Alto, Spain. The spectropolarimetry used the low-resolution B200 grism coupled with a 1″5 slit, giving a spectral range 3300–8900 Å, a dispersion of ~4.7 Å/pix, and a full width at half maximum resolution of 21.0 Å. Spectropolarimetry from Calar Alto was obtained on 2014 January 28 (day −6), February 03 (day 0, already published in Patat et al. 2015), and March 08 (day 33). We also used broadband polarimetry taken with the Hiroshima One-shot Wide-field Polarimeter (HOWPol, Kawabata et al. 2008) around optical maximum, as published by Kawabata et al. (2014).

3. Analysis

Figure 2 presents the wavelength dependence and time evolution of the new *HST* data points, along with ground-based polarimetry. The *HST* data can be compared to ground-based polarimetry acquired around optical maximum to study the temporal evolution of the polarization. Broadband polarimetric observations of SN 2014J taken on January 22.4 (−11 days relative to *B*-band maximum), January 27.7 (−6 days), February 16.5 (+14 days), February 25.6 (+23 days), and March 7.8 (+33 days) detected no variability (Kawabata et al. 2014). Spectropolarimetry on 2014 January 28 (−6 days), February 03 (+0 day), and March 08 (+33 days) indicates no temporal evolution either (Patat et al. 2015). The continuum polarization of SN 2014J reaches about 6.6% at 0.4 μm, and the variability in ground-based data was less than 0.2%, except at the bluest end where the data were noisy but are still consistent with constancy (Patat et al. 2015). At the 0.2% level, the intrinsic polarization of the SN becomes significant (Wang et al. 2008). This makes it difficult to determine the contribution from circumstellar dust. We conclude that the overall high level of polarization at early times is due to interstellar dust, and that there is no detectable variability at early times down to the 0.2% level.

3.1. Interstellar Polarization

The "Serkowski Law" provides an empirical wavelength dependence of optical/near-infrared (NIR) interstellar polarization (Serkowski et al. 1975). It can be written as:

$$p(\lambda)/p_{max} = \exp[-K \ln^2(\lambda_{max}/\lambda)], \quad (6)$$

where λ_{max} is the wavelength of the maximum polarization $p(\lambda_{max})$ and K is a parameter describing the width of the polarization peak. We fitted this relation to optical spectropolarimetry at maximum light. The interstellar polarization wavelength dependence toward SN 2014J exhibits a very steep
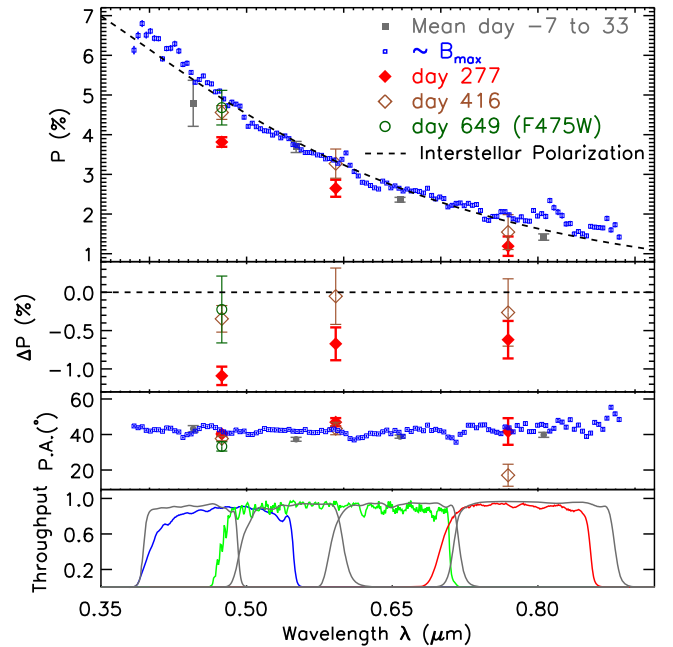

Figure 2. From top to bottom: the first panel presents the optical imaging polarimetry of SN 2014J taken with *HST* ACS/WFC on day 277, day 416, and day 649, compared with earlier broadband polarization between day 7 and day 33 (gray, solid squares, Kawabata et al. 2014) and spectropolarimetry near *B*-band maximum (blue, open squares, Patat et al. 2015). The dashed line presents the "Serkowski law" fit of the interstellar polarization; the second panel gives the difference between our *HST* polarimetry and the interstellar polarization; the third panel displays the corresponding polarization position angles; the bottom panel illustrates the filter transmission curves for the broadband polarimetry (Kawabata et al. 2014) (gray lines), and the *HST* F475W (blue line), broad F606W (green line), and F775W (red line) filter band measurements. The *HST* data on day 277 exhibit a conspicuously different degree of polarization in all three filter bands compared to the other data sets. At later epochs, the polarization returns to the values at maximum light.

increase from the red to the blue (Kawabata et al. 2014; Patat et al. 2015). The position of the polarization peak cannot be determined due to the lack of UV data. Therefore, we employ the canonical value $K = 1.15$, according to Serkowski et al. (1975), and obtain a reasonable fit with $\lambda_{max} = 0.25$ μm and $p(\lambda_{max}) = 8.1\%$. Our fitting to Serkowski's law is shown in the first panel of Figure 2, together with the polarimetry of SN 2014J. Extrapolation to the effective wavelengths of the F475W, F606W, and F775W filters yields values of 4.9%, 3.3%, and 1.8%, respectively for the interstellar polarization.

3.2. Polarimetry of Light Scattered from an SN

In the *HST* data from day 277, the *F475W*-band degree of polarization has changed from 4.9% near maximum light to 3.8%, and no obvious change in PA has been observed. A stability check of the *HST* polarimetry will be presented in Section 3.3. The *F475W*-band data have the highest *S/N*. The data in the *F606W* and *F775W* bands also show different degrees of polarization. The data on day 416, however, are consistent with those from maximum light. Polarimetry at later epochs suffers from larger uncertainties as the SN fades; however, it is still broadly consistent with the interstellar polarization. Sparks & Axon (1999) fitted the errors of the polarization degree and the polarization PA with the average S/N ratio and the degree of polarization:

$$\log_{10}(\sigma_p/p) = -0.102 - 0.9898 \log_{10}(p \langle S/N \rangle_i)$$
$$\log_{10} \sigma_{\mathrm{PA}} = 1.415 - 1.068 \log_{10}(p \langle S/N \rangle_i). \quad (7)$$

For example, exposures at each polarizer achieving $\langle S/N \rangle_i \sim 500$ yield relative uncertainties $\sigma_p/p = 3.3\%$, 4.9%, and 9.0% in the *F475W*, *F606W*, and *F775W* bandpasses, respectively. For $\langle S/N \rangle_i \sim 100$, the corresponding values are $\sigma_p/p = 16\%$, 24%, and 44% in the *F475W*, *F606W*, and *F775W* bandpasses, respectively. The exposure time in the *F475W* band at later epochs was longer, and the average S/N ratio for the SN point source is estimated as 700, 450, 190, 100, 40, and 30, leading to values in (σ_p/p) of 3.1%, 4.6%, 11%, 21%, 50%, and 70%, from V1 to V6, respectively. The fractional errors are also in good agreement with the errors derived with Equation (4) and presented in Table 2. The polarization PA at all visits are broadly consistent with the average polarization PA 42.2 ± 0.3 deg derived around maximum light (Patat et al. 2015).

Differences in observed polarization on day 277 can be explained with a non-uniform distribution of circumstellar dust in the vicinity of SN 2014J. Modeling the observed polarization in terms of dust scattering of SN light is usually an ill-defined problem due to the lack of knowledge about the geometric distribution of the dust and its absorption and scattering properties. A unique solution is usually very difficult to achieve; however, important constraints can be deduced based on simple and robust models.

The most efficient configuration for producing polarized light is given by a single dust clump near the location of the SN but offset from the SN on or close to the plane of the sky. In such a configuration, the light incident on the dust clump is scattered near 90° and can be polarized at the 50%–100% level. The degree of polarization depends on the details of the geometry and optical depth of the dust clump. For simplicity (and without loss of much generality), the amount of scattered light can be written as the following equation:

$$L_{\mathrm{scat}}(t) = \tau \frac{\delta\Omega}{4\pi} \Phi(\theta) \int L(t - t_e) K(t - t_d) dt_e, \quad (8)$$

where t and t_e give the time of observation and the time since SN explosion, respectively, τ is the optical depth along the scattering direction in the circumstellar cloud, $\delta\Omega$ is the solid angle that the clump subtends toward the SN, $L(t)$ is the luminosity of the SN as a function of time, t_d denotes the light traveltime from the SN to the center of the dust clump, θ gives the scattering angle, and $\Phi(\theta)$ is the scattering phase function.

We assume that dust scattering follows the Henyey–Greenstein phase function (Henyey & Greenstein 1941):

$$\Phi(\theta) = \frac{1}{4\pi} \frac{1 - g^2}{(1 + g^2 - 2g \cos\theta)^{3/2}}, \quad (9)$$

where $g = \overline{\cos\theta}$ is a measure of the degree of forward scattering and computed by Laor & Draine (1993). The function K is determined by the details of the dust distribution. It reduces to an infinitely narrow Dirac δ-function for an infinitely thin layer of dust lying on the surface of the light travel iso-delay surface (see Patat 2005). For a more realistic distribution, K reduces to a broader function whose width characterizes the radial extent of the clump. The lack of a precise geometric model of the dust clump leads us to approximately describe the scattering properties of the clump with (a) an infinitely narrow Dirac δ-function and (b) a Gaussian function of the form $K(t) = \frac{1}{\sqrt{2\pi}\,\sigma_t} \exp(-\frac{t^2}{2\sigma_t^2})$. Here, $\sigma_t \times c$ characterizes the radial extent of the clump and τ can be the average optical depth of the clump, which is linearly related to the average column depth in the case of an optically thin clump. In the following, we use the more restrictive Dirac δ-function assumption to deduce the minimal amount of dust responsible for the late-time variations in polarization. In addition, we also calculate this quantity for a radially extended dust clump approximated by a Gaussian function with $\sigma = 20$ light days.

The degree of polarization is then

$$p = \frac{L_{\mathrm{scat}}(t)}{L(t) + L_{\mathrm{scat}}(t)} \Theta(\theta), \quad (10)$$

where $\Theta(\theta)$ is the polarization of light scattered with scattering angle θ. We adopt the Mie scattering (Mie 1908) model for dust particles of radius $a = 0.1 \,\mu$m, comparable to the wavelengths of the filter bands. The scattering phase functions and optical properties of dust particles were calculated using the OMLC Mie Scattering Calculator.[12]

Dust located on the iso-delay light surface for a given epoch will produce scattered flux. The total mass of the dust responsible for the scattering gives:

$$M_{\mathrm{dust}} = n_{\mathrm{gr}} V_{\mathrm{gr}} \rho_{\mathrm{gr}} dV, \quad (11)$$

where n_{gr} is the dust grain number density. Here, V_{gr} describes the volume of a single dust grain and can be written as $V_{\mathrm{gr}} = A_{\mathrm{gr}} l_{\mathrm{gr}}$, where l_{gr} represents the effective length perpendicular to a grain's geometric cross-section with an area of A_{gr}. The volume of the dust cloud gives $dV = r^2 \sin\theta d\theta d\phi dr$, where $r = ct_d/(1 - \cos\theta)$ gives the distance from the SN to a dust cloud, and t_d denotes the time within which the SN radiation reaches the dust cloud. The optical depth of this dust cloud can be expressed as follows:

$$\tau = n_{\mathrm{gr}} A_{\mathrm{gr}} Q_{\mathrm{ext}} dr, \quad (12)$$

where Q_{ext} gives the extinction efficiency for dust grains. Under the assumption of an infinitely narrow Dirac δ-function dust
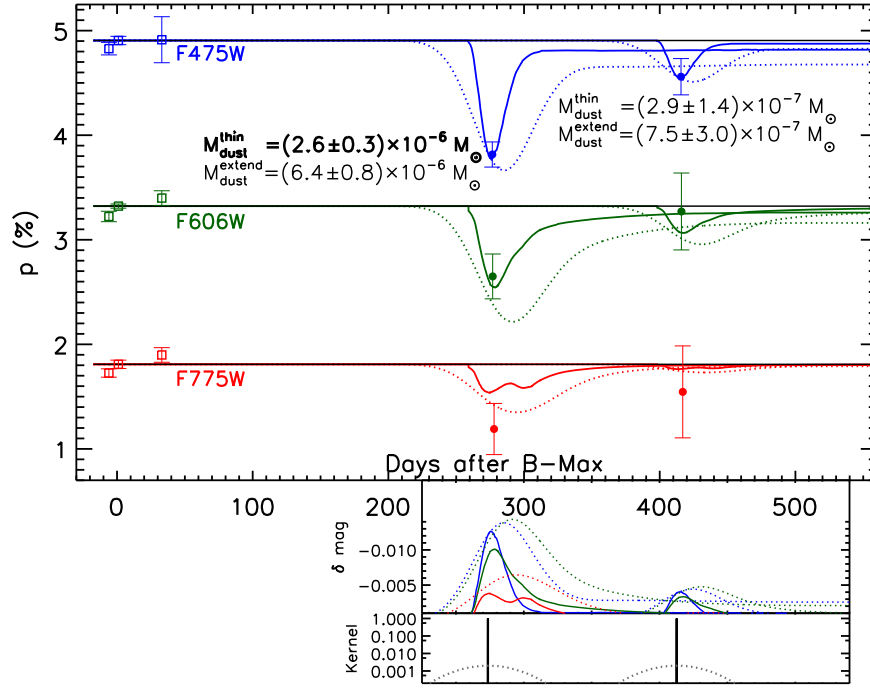

Figure 3. Single-dust-clump models of the late-time polarimetry of SN 2014J. In the upper panel, the blue, green, and red lines are for $F475W$, $F606W$, and $F775W$-band data, respectively. The straight horizontal lines in each color indicate the average polarization (Patat et al. 2015) in each filter. The solid lines represent the models for an infinitely thin dust distribution, and the dashed lines illustrate the models for a radially extended dust clump approximated by a Gaussian function with $\sigma = 20$ light days. The higher of the two smaller panels at the bottom shows the expected contribution to the integrated light curves by the hypothetical silicate dust clump, which can account for the observed polarization evolution. The lower of these two panels describes the infinitely thin (Dirac δ-function) and Gaussian dust kernels. All panels share the same time axis.

cloud, the amount of scattered photons can be expressed as:

$$L_{\mathrm{scat}}(t) = \omega\tau L(t - t_e)\sin\theta\delta\theta\delta\phi\Phi(\theta). \quad (13)$$

The amount of polarized scattered light can therefore be used to infer the optical depth and mass of the scattering dust cloud. When the light from the SN is still dominant over the scattered light by the circumstellar dust cloud, i.e., $L(t) \gg L_{\mathrm{scat}}(t)$, and recalling Equations (10), we can rewrite (13) as:

$$\tau = p\frac{1}{\omega}\frac{L(t)}{L(t - t_e)}\frac{1}{\delta\theta}\frac{1}{\delta\phi}\frac{1}{\Phi(\theta)}\frac{1}{\Theta(\theta)}\frac{1}{\sin\theta}, \quad (14)$$

where ω denotes the grain albedo.

The mass of the dust cloud is then given by:

$$M_{\mathrm{dust}} = \tau l_{\mathrm{gr}}\rho_{\mathrm{gr}}\frac{1}{Q_{\mathrm{ext}}}r^2\sin\theta d\theta d\phi. \quad (15)$$

Without knowing the exact shape of the dust grains, it is reasonable to replace l_{gr} with the radius of the dust grain, a. The grain albedo ω can be expressed as $\omega = Q_{\mathrm{scat}}/Q_{\mathrm{ext}}$, where Q_{scat} and Q_{ext} give the scattering and the extinction efficiency, respectively. We rewrite ωQ_{ext} as Q_{scat} and adopt the values computed for various dust models (see the following paragraph). The lack of information regarding the geometric size of the dust cloud makes it reasonable to assume that the scattering kernel is a function of the geometric width of the clump. For a single clump and a thin, Dirac δ-function kernel, combining Equations (14) and (15), we found the following

constraints on the dust mass:

$$M_{\mathrm{dust}}^{\mathrm{thin}} \geqslant 1.4 \times 10^{-7}M_\odot\frac{p}{1\%}\left[\frac{L(0)/L(t_d)}{1.0 \times 10^{-4}}\right]\left[\frac{ct_d/(1 - \cos\theta)}{1\ l.y.}\right]^2$$
$$\times \frac{1}{Q_{\mathrm{scat}}}\frac{\rho_{\mathrm{gr}}}{2.5\ \mathrm{g\ cm^{-3}}}\frac{a}{0.1\ \mu m}\frac{1}{\Phi(\theta)}\frac{1}{\Theta(\theta)}, \quad (16)$$

where p is the observed amount of polarization evolution and ρ_{gr} is the physical density of the dust grains.

For SN 2014J, we have identified a strong polarization anomaly at day 277 after B-maximum, which shows a polarization that differs in all filter bands from the polarization observed around optical maximum and the polarization at later times taken by the same program. We applied the above model to the observed data to deduce the amount of dust needed to produce the observed polarization at day 277. The results for Mie scattering by "astronomical silicate" (Draine & Lee 1984; Laor & Draine 1993; Weingartner & Draine 2001) are shown in Figure 3 for all three bands. Based on our measurement through $F475W$ with the highest S/N ratio, a minimum mass of silicate dust of $2.4 \times 10^{-6}\ M_\odot$ is needed to reproduce the observed polarization evolution, at a scattering angle of $114^{+5°}_{-5}$ with respect to the line of sight. We also considered graphite and Milky Way dust, which yield minimal dust masses of $(3.6 \pm 0.4) \times 10^{-6}\ M_\odot$ and $(3.2 \pm 0.4) \times 10^{-5}\ M_\odot$, respectively. Table 3 summarizes the amount of dust inferred from the difference in the polarization degree between days 277 and 416. The required minimal dust masses were derived from Equation (16). The scattering angles were then obtained from the same equation when the masses acquire its minimum value;

Table 3
Minimal Dust Masses Implied by the Observed Polarization

Epoch (Days)	Dust	θ_{max} (°)	r (cm)	Mass (θ_{max}) ($M_{\odot}$)	Mass ($\theta_{90°}$) ($M_{\odot}$)
$t = 33$[a]	Milky Way	100^{+4}_{-4}	$7.3^{+0.5}_{-0.4} \times 10^{16}$	$(-0.1 \pm 2.7) \times 10^{-6}$	$(-0.1 \pm 2.8) \times 10^{-6}$
	Silicate	114^{+5}_{-5}	$6.1^{+0.4}_{-0.3} \times 10^{16}$	$(-0.1 \pm 2.1) \times 10^{-7}$	$(-0.1 \pm 3.2) \times 10^{-7}$
	Graphite	92^{+5}_{-5}	$8.3^{+0.7}_{-0.6} \times 10^{16}$	$(-0.1 \pm 3.0) \times 10^{-7}$	$(-0.1 \pm 3.0) \times 10^{-7}$
$t = 277$	Milky Way	100^{+4}_{-4}	$6.1^{+0.4}_{-0.3} \times 10^{17}$	$(3.2 \pm 0.4) \times 10^{-5}$	$(3.6 \pm 0.4) \times 10^{-5}$
	Silicate	114^{+5}_{-5}	$5.1^{+0.3}_{-0.3} \times 10^{17}$	$(2.5 \pm 0.3) \times 10^{-6}$	$(3.7 \pm 0.4) \times 10^{-6}$
	Graphite	92^{+5}_{-5}	$6.9^{+0.6}_{-0.5} \times 10^{17}$	$(3.6 \pm 0.4) \times 10^{-6}$	$(3.6 \pm 0.4) \times 10^{-6}$
$t = 416$	Milky Way	100^{+4}_{-4}	$9.2^{+0.6}_{-0.5} \times 10^{17}$	$(3.7 \pm 1.9) \times 10^{-6}$	$(4.1 \pm 2.1) \times 10^{-6}$
	Silicate	114^{+5}_{-5}	$7.7^{+0.5}_{-0.4} \times 10^{17}$	$(2.9 \pm 1.4) \times 10^{-7}$	$(4.3 \pm 2.2) \times 10^{-7}$
	Graphite	92^{+5}_{-5}	$1.0^{+0.1}_{-0.1} \times 10^{18}$	$(4.1 \pm 2.1) \times 10^{-7}$	$(4.2 \pm 2.1) \times 10^{-7}$

Note.
[a] The negative masses on day 33 are due to an opposite sign of the differences from the interstellar foreground polarization compared to day 277 and day 416.

they are slightly dependent on the adopted distribution model, but always near 90°. Uncertainties were estimated through a Monte-Carlo procedure by adding Gaussian errors to the parameter values. Because systematic errors are also present, the resulting error margins are only lower limits of the real uncertainties of the single-dust-clump model. Figure 4 provides a schematic view of the single dust clump model, which explains the time-dependent polarization of SN 2014J.

A single dust clump close to the plane of the SN leads to the largest possible polarization. Any more complex geometric distribution of the dust will be less efficient in polarizing scattered light from the SN, and therefore more dust will be needed to achieve the same degree of polarization. Nonetheless, the single-dust-clump model can provide useful insights even for a more complicated geometry, such as a non-uniform dust distribution. In such a case, the polarization will be related to the fluctuations of the column depth of dust to the SN.

For dust distributed in a torus viewed edge-on, the amount of dust needed is $\sim 2\pi/\delta\theta$ times larger than demanded by the single dust clump model with an angular size $\delta\theta$. Figure 5 presents the amount of dust required to account for the observed change in polarization at different scattering angles. This allows the single dust clump to move along the iso-delay light surface in Figure 4 and provides a more universal description of the implied dust mass. The minimum amount of dust that is compatible with a torus geometry is still consistent with constraints from NIR observations, i.e., $10^{-5} M_{\odot}$ inside a radius 1.0×10^{17} cm (Johansson et al. 2017). If we model the polarization in terms of a non-uniform spherical shell, the required mass will be either larger than or on the order of $4\pi/\delta\theta^2$ times that of a single dust clump.

3.3. Stability Check of the HST Polarimetry

HST has obtained only few other polarimetric observations of point sources that could be used to assess the quality of the observations of SN 2014J. Therefore, in order to test the stability of *HST* polarimetry, we have also measured the polarization of a number of stars and nebular sources in the surrounding *HST* WFC field. We assume that the polarization of the field sources other than SN 2014J is due to polarization from foreground dust, and is therefore time-invariant. These stars and nebulae are
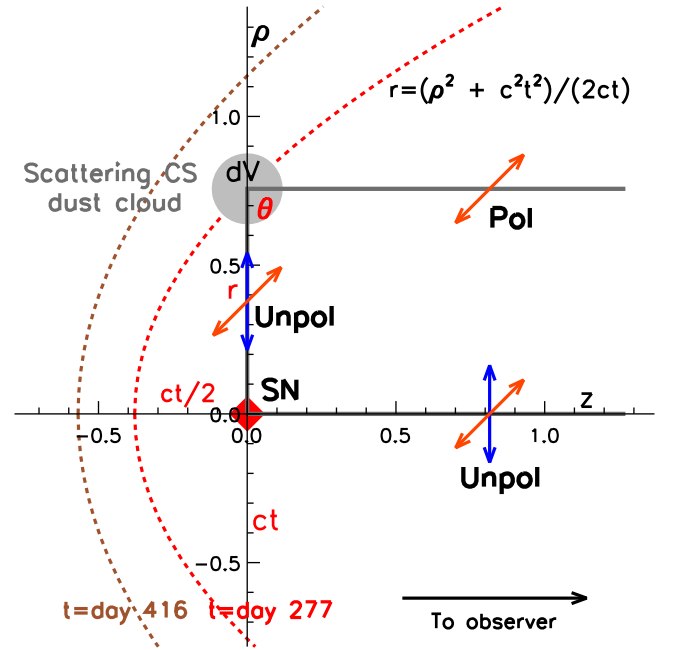

Figure 4. Schematic diagram illustrating the geometrical configuration of a circumstellar light echo around a supernova. The diagram describes the contribution from photons scattered by a circumstellar dust cloud at a large angle (i.e., $\theta = 90°$) and the time-variant polarization of the SN 2014J. The abscissa and ordinate represent the foreground distance (z) in and projected distance on the sky (ρ), respectively. Both z and ρ are in light years. Paraboloids represent the iso-delay light surfaces at different epochs (as labeled), "Pol" and "Unpol" denote "polarized light" and "unpolarized light," respectively, as seen by the observer located outside the right edge of the figure.

identified in Figure 6. The evolution of their polarization between days 277 and 416 is visualized in Figure 7.

For each source and epoch, we measured the flux with three different aperture sizes. We used the spreads (full ranges, denoted as "*dq* range" and "*du* range") in each such set of three measurements to characterize their reliability. Bright and highly polarized sources should be less affected by noise and hence exhibit a smaller spread, making them useful references to check the stability of *HST* polarimetry. Because of the small number of measurements (three) per source and epoch, which renders standard deviations relatively meaningless, we use these spreads as proxies of the data quality and instrumental
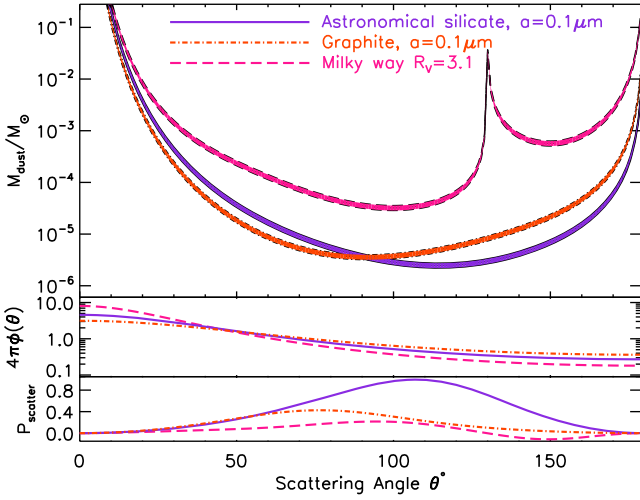
Figure 5. The dust mass required to produce the observed level of polarization as a function of scattering angle caused by the dust clump's position along the iso-delay surface at day 277 (when the deviant polarization was measured), and as depicted in Figure 4, which shows the case of the $\theta = 90°$. In the upper panel, the cases of silicate, graphite, and Milky Way dust are represented by a solid purple, dotted–dashed orange, and dashed pink line, respectively. The scattering-angle dependency of scattering phase functions and polarization efficiencies obtained from Weingartner & Draine (2001) are overplotted in the middle and bottom panel, respectively.

stability. SN 2014J and the four brightest other sources in the field are marked with colored circles in Figure 6. Circular apertures of 0″.35, 0″.40, and 0″.45 were used to measure faint and point sources, while 0″.65, 0″.70, and 0″.75 were applied for extended sources.

In the upper (lower) left panel of Figure 7, the median of the individual measuring errors in dq (du) with the three apertures is plotted versus the dq (du) range. The sources are identified in Figure 6. As shown in Table 4, the individual errors of the three measurements of each source are very similar because the apertures differ by only $\pm0″.05$ from the median size. Additional measurements of fainter field sources appear as various gray symbols; they are the same in the two left panels of Figure 7. The individual errors scale with the spread and vice versa. This is expected for well-behaved data. Therefore, these graphs confirm the sanity of the data and the method. However, the spread is mainly a systematic uncertainty introduced by the usage of different apertures, while the ordinate illustrates photometric errors propagated to the measurement of dq and du.

In the du versus dq panel of Figure 7, a significant separation of SN 2014J from the error-weighted mean of all measurements on all sources would demonstrate that the polarization of the SN was not constant and evolved with time. However, the overall scatter of all field sources is dominated by the large errors of the faint sources (gray dots). Therefore, we selected those sources whose spreads (ranges) in dq and du are less than three times those of SN 2014J. Only sources 1 & 2 satisfy this criterion. For the two next fainter sources, 3 & 4, either the spread in dq or du are already larger than this limit. Other sources were not included because, for each of them, the spreads exceed the threshold in both dq and du.

The measured polarizations of the four brightest comparison sources are included in Table 4. The error-weighted mean dq and du values of the two brightest field sources were calculated to be $\overline{dq}^w = -0.05\% \pm 0.03\%$ and $\overline{du}^w = 0.32\% \pm 0.04\%$,

respectively. The results for sources 1–4, $\overline{dq}^w = -0.06\% \pm 0.03\%$ and $\overline{du}^w = 0.33\% \pm 0.04\%$ are consistent with those for the two brightest sources only. For the calculation of the error-weighted means of dq, du, and their associated errors, we used the following relations:

$$\overline{x}^w = \frac{\Sigma_{i=i}^N x_i/\sigma_i^2}{\Sigma_{i=i}^N 1/\sigma_i^2}, \; \sigma_x^w = \sqrt{\frac{1}{\Sigma_{i=i}^N 1/\sigma_i^2}}, \qquad (17)$$

where x and σ denote the measurement and error, respectively, of dq or du. N is the total number of the individual measurements which are numbered by the index i. Uncertainties given by σ_x^w do not account for the systematic uncertainty introduced by the usage of different apertures. We estimated this systematic error by calculating the error-weighted standard deviation of the individual measurements:

$$\sigma_x^s = \sqrt{\frac{\Sigma_i^N (x_i - \overline{x}^w)^2/\sigma_i^2}{\frac{N-1}{N}\Sigma_{i=1}^N 1/\sigma_i^2}}, \qquad (18)$$

which gives $\sigma_{dq}^s = 0.07\%$, $\sigma_{du}^s = 0.03\%$ including source 1 & 2, and $\sigma_{dq}^s = 0.10\%$, $\sigma_{du}^s = 0.08\%$ for sources 1−4. The errors of the error-weighted means shown in Figure 7 were estimated by adding σ_x^w and σ_x^s in quadrature.

The final estimated error-weighted mean and associated error are $\overline{dq}^w = -0.05\% \pm 0.07\%$ and $\overline{du}^w = 0.32\% \pm 0.05\%$ when based on sources 1 & 2, and $\overline{dq}^w = -0.06\% \pm 0.10\%$ and $\overline{du}^w = 0.33\% \pm 0.09\%$ if sources 3 & 4 are also included. As shown in Figure 7, the difference in polarization of SN 2014J between day 277 (V1) and day 416 (V2), i.e., $dq = (0.57 \pm 0.12)\%$, $du = (0.46 \pm 0.17)\%$, deviates by more than three times its error from the error-weight mean value calculated from bright sources in the field. The error-weighted mean values of dq and du—including all the marked fainter sources, as well as those excluded from the previous analysis—are $dq = -0.06\% \pm 0.03\%$ and $du = 0.16\% \pm 0.03\%$. That is, unlike SN 2014J, there are no general significant systematic differences in polarization between epochs V1 and V2. Additionally, the polarization measured in different regions of the CCD has previously been shown to agree to within 0.2% (Sparks et al. 2008). Therefore, we conclude that the observed change in polarization of the SN is not an artifact of the instrument.

4. Discussion

Around optical maximum, as well as after day 416, the measured polarizations are the same to within the errors, but different from those on day 277. The deviated degree of polarization on day 277 can be explained by light from SN scattered by circumstellar ejecta of $\gtrsim 5 \times 10^{17}$ cm ($\sim$0.5 light years) from SN 2014J. Compared to the dust detected at day 277, the amount of dust at even closer distances from the SN is constrained by the absence, at the 0.2% level, of variability of the early polarization. Following Yang et al. (2017) and the relations between two-dimensional light echoes and three-dimensional scattering dust distributions (Chevalier 1986; Sparks 1994; Sugerman 2003; Tylenda 2004; Patat 2005), we briefly define the geometry of circumstellar light echoes used through this paper, also sketched in Figure 4. The SN is placed at the origin of the plane of the sky, a scattering volume element dV lies at distance r from the SN, and z gives
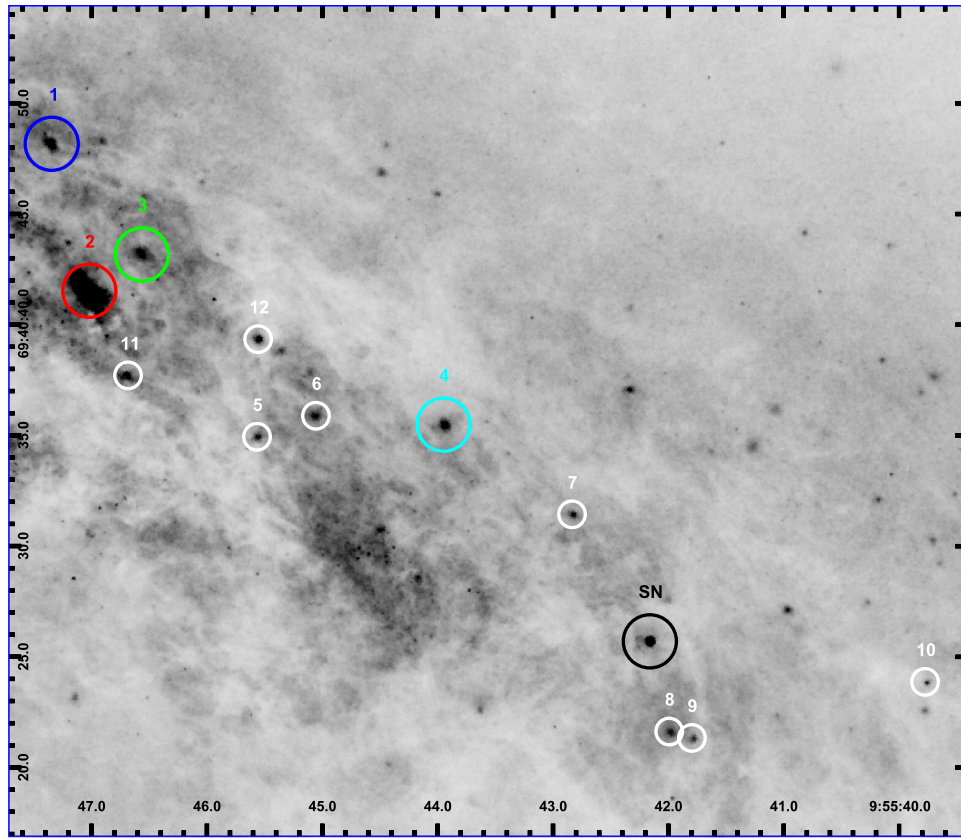
Figure 6. The bright sources in the *HST* images used for determining the stability of the polarization measurements. Each source has been monitored with three aperture sizes (cf. Table 4). The SN is circled in black. The four brightest nearby sources are circled in large blue, green, red, and cyan, respectively, and are labeled with ID numbers also used in Table 4. Fainter sources with larger errors are circled in white.

the foreground distance of the scattering volume element along the line of sight. The iso-delay light surface of the light echo can be approximated very well by a paraboloid whose focus coincides with the SN. We define ρ as the distance from a scattering volume element to the SN, projected perpendicular to the line of sight (the z direction). The iso-delay light surface gives:

$$r = \frac{1}{2}\left(\frac{\rho^2}{ct} + ct\right),\qquad(19)$$

where t is the time since the SN radiation burst and c denotes the speed of light. The scattering angle θ is therefore given by:

$$\cos\theta(\rho, t) = z/(z + ct).\qquad(20)$$

We use the single-clump hypothesis and the scattering angle of 114° with respect to the line of sight that is implied by the minimum amount of astronomical silicate compatible with the observed change in polarization. From Equations (19) and (20), it then follows that the day 33 observations imply less than $2.6 \times 10^{-7}\,M_\odot$ at a distance around 23.5 light days (7.3×10^{16} cm). Similarly, the *HST* observations on day 416 constrain the mass of a single dust clump to less than $4.0 \times 10^{-7}\,M_\odot$ (1σ) at a distance around 296 light days (7.7×10^{17} cm). Approximating the radial distribution of the clump with a Gaussian function of $\sigma_t = 20$ light days generally increases the amount of dust by a factor of 2–2.5 with respect to the above assumed δ function. A single dust clump is, of course, an oversimplification. The lower limit it places on the mass on day 277 may be much larger if the dust is more

uniformly distributed, either in a thin slab in the plane of the sky at the location of the SN 2014J or in a more radially extended volume.

The interpretation of these data is highly model-dependent, but the difference of polarization between these epochs and at the SN maximum requires there to be either no dust at distances of $\sim 6.1 \times 10^{16}$ cm (day 33) and $\sim 7.7 \times 10^{17}$ cm (day 416) based on Equation (16) (see, i.e., Table 3), or the dust distribution at these distances is extremely uniform, such that the opacity fluctuation on the plane of sky is less than $\sim 0.002 \pm 0.06$ at day 33, and less than $\sim 0.0004 \pm 0.0002$ at day 416, based on Equation (14) and assuming $\delta\theta \sim \delta\phi \sim 0.1$. After day ~ 649, the errors of the polarization measurements are much larger, but the results are still consistent with the polarization at maximum light. Therefore, between day ~ 416 and ~ 1181, the light from SN 2014J did not encounter significant amounts of dust.

4.1. Implications for the Progenitor

Mass loss through steady stellar wind produces an axially symmetric ambient medium around the line of sight. For an unresolved source, the resultant circumstellar mass profile would lead to a cancellation of the vectors of the scattered radiation, resulting in zero net circumstellar polarization. Therefore, polarimetry cannot independently constrain the mass of material homogeneously distributed around an SN. Comprehensive observational studies on SN 2014J disfavor the single-degenerate models with a steady mass loss. The absence of a stellar progenitor in pre-explosion images has safely ruled
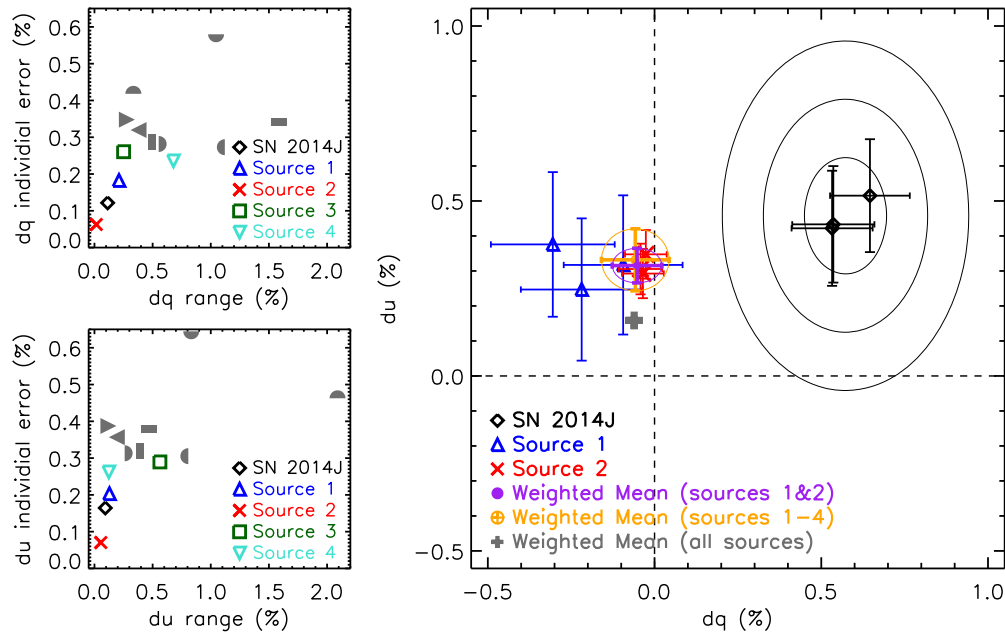
Figure 7. Sources used to check the stability of *HST* polarimetry. The left panels present, for each source, the median of the individual errors of the polarization measurements with three different apertures as a function of spread (ranges) of the measurements with these apertures. Similar measurements of other faint field sources are shown by various gray symbols, which are the same in the upper and lower panels. In the right panel, the horizontal and vertical axes represent the differences between the *q* and *u* values, respectively, measured on days 416 and 277. SN 2014J and the two brightest other sources (1−2) are marked with black and colored circles as in Figure 6. The error-weighted mean difference including comparison sources 1 & 2, sources 1−4, and all the other fainter sources marked in Figure 6 are indicated by the purple dot, the orange circle with plus sign, and the gray cross, respectively. The brightest source, plotted in red, together with the error-weighted mean, reveals no time evolution at the 0.3% level. Black ellipses show one-, two-, and three-sigma contours centered at the error-weighted mean of SN 2014J. They demonstrate that the variation in polarization of the SN deviates by more than three times its errors from the variation of the field sources (assumed to be intrinsically constant). This comparison suggests a genuine evolution of the polarization of SN 2014J between days 277 and 416 (epochs V1 and V2).

out the possibility of red giant donor star (Kelly et al. 2014). The non-detection in X-rays and radio shows a lack of pre-existing material to be heated in vicinity of SN 2014J (Margutti et al. 2014; Pérez-Torres et al. 2014). A combination of numerical models and a late-time optical spectrum of SN 2014J (at 315 days after the explosion) has constrained the H-rich unbounded material to be less than $0.0085 M_\odot$ (Lundqvist et al. 2015). The *Spitzer* mid-infrared observations constrain the amount of dust around SN 2014J to be $\lesssim 10^{-5} M_\odot$ within a radius of 2.0×10^{17} cm (Johansson et al. 2017).

The gas-to-dust mass ratio for the 8 kpc region around the center of M82 is $\sim$200 (Kaneda et al. 2010). Depending on the dust properties in M82, the mass of circumstellar dust clouds depends on the nature and evolution of the progenitor system. From Table 3, we derive a total minimal mass (dust+gas) of the CSM responsible for the deviations in late-time degree of polarization to be $\gtrsim 5 \times 10^{-4} M_\odot$ at a distance of $\sim 5.1 \times 10^{17}$ cm ($\sim$197 light days), and similar constraints on the mass of the CSM are $\sim 2 \times 10^{-5} M_\odot$ and $\sim 6 \times 10^{-5} M_\odot$ at $\sim 6.1 \times 10^{16}$ cm (day 33) and $\sim 7.7 \times 10^{17}$ cm (day 416), respectively. Therein, "CSM" denotes matter lost by the progenitor system whereas "ISM" is matter that just happens to be close the location of the progenitor but is not related to it. This distinction does not include any a priori implications for the distance of such matter from the progenitor.

4.1.1. Single-degenerate Models

The distance of $\sim 5.1 \times 10^{17}$ cm (197 light days) between the dust and the SN can be compared to a putative nova outburst of the progenitor prior to the SN explosion. Recurrent nova explosions result from a near-Chandrasekhar mass WD

accreting at $\sim (0.1-3) \times 10^{-7} M_\odot$ yr^{-1} and experiencing unsteady H burning at its surface (e.g., Iben 1982; Starrfield et al. 1985; Livio & Truran 1992; Yaron et al. 2005). For a typical nova ejection speed of $v_{\rm ej} \sim 1000$ km s^{-1}, the inferred distance between the dust cloud and SN 2014J is consistent with an eruption $t_{\rm ex} \sim 160$ years ago. If the nova outburst was brief, the ejected mass is likely distributed in a thin, clumpy shell. It is also possible that the high-speed shell ejection is concurrent with a slower wind from the donor star, and any matter surrounding the progenitor was swept up by the most recent blast wave (see, e.g., Wood-Vasey & Sokoloski 2006). These mechanisms in the single-degenerate channel can explain the absence of dust closer to and farther away from SN 2014J. We refer to Margutti et al. (2014) for a thorough discussion on the progenitor configuration for single-degenerate models.

In some other variants of the single-degenerate model, the SN may have exploded inside a planetary nebula shell (Wang et al. 2004; Tsebrenko & Soker 2013, 2015). Numerical models of a type Ia SN inside a planetary nebula may explain the observed morphologies of the *Kepler* and G299.2−29 supernova remnants (SNRs, Tsebrenko & Soker 2013) and G1.9+0.3 SNR (Tsebrenko & Soker 2015). The double-shock structure in the G1.9+0.3 SNR can be reproduced well by the interaction of type Ia SN ejecta with the planetary nebula shell including two or three dense clumps (Tsebrenko & Soker 2015). The observed mean radius of the G1.9+0.3 SNR is about 2 pc, and in this case, simulations imply the total mass in the planetary nebula and the clumps to be $\approx 0.09 M_\odot$. The size and total mass of the planetary nebula shell vary in different cases, and we consider that the mass and the distance of the CSM constrained by our polarimetry of SN 2014J are also broadly

Table 4
Polarizations of Other Bright Sources in the *HST* ACS/WFC Field

	R.A.(J2000)	Decl. (J2000)	Aperture (Radius in ″)	q^1	q^2	u^1	u^2	I^a	I^b
	(h:m:s)	(d:m:s)		(%)	(%)	(%)	(%)	(counts s^{-1})	(counts s^{-1})
SN 2014J	09:55:42.11	69:40:25.90	0.35	-0.61 ± 0.08	-1.15 ± 0.12	-3.79 ± 0.08	-4.22 ± 0.12	2695.0 ± 1.6	399.3 ± 0.3
			0.40	-0.60 ± 0.08	-1.13 ± 0.12	-3.82 ± 0.08	-4.24 ± 0.12	2736.6 ± 1.6	415.2 ± 0.3
			0.45	-0.57 ± 0.08	-1.22 ± 0.12	-3.82 ± 0.08	-4.34 ± 0.12	2775.3 ± 1.6	432.8 ± 0.4
Source 1	09:55:47.29	69:40:48.37	0.65	0.41 ± 0.17	0.72 ± 0.10	-0.80 ± 0.17	-1.18 ± 0.10	654.0 ± 0.8	644.3 ± 0.4
			0.70	0.42 ± 0.17	0.64 ± 0.10	-1.03 ± 0.16	-1.28 ± 0.10	686.8 ± 0.8	676.2 ± 0.5
			0.75	0.46 ± 0.16	0.55 ± 0.09	-1.13 ± 0.16	-1.45 ± 0.09	720.6 ± 0.8	707.6 ± 0.5
Source 2	09:55:46.97	69:40:41.73	0.65	3.55 ± 0.06	3.60 ± 0.03	-2.98 ± 0.06	-3.29 ± 0.03	5362.3 ± 2.2	5373.5 ± 1.3
			0.70	3.50 ± 0.06	3.53 ± 0.03	-2.95 ± 0.06	-3.24 ± 0.03	5573.6 ± 2.3	5583.6 ± 1.3
			0.75	3.43 ± 0.06	3.46 ± 0.03	-2.89 ± 0.06	-3.23 ± 0.03	5779.5 ± 2.3	5787.4 ± 1.3
Source 3	09:55:46.51	69:40:43.37	0.35	1.18 ± 0.26	1.33 ± 0.15	-2.64 ± 0.26	-2.81 ± 0.15	272.5 ± 0.5	274.8 ± 0.3
			0.40	1.39 ± 0.24	1.38 ± 0.14	-2.52 ± 0.24	-2.85 ± 0.13	325.4 ± 0.5	329.8 ± 0.3
			0.45	1.15 ± 0.23	1.39 ± 0.13	-2.22 ± 0.22	-2.96 ± 0.13	370.6 ± 0.6	375.2 ± 0.3
Source 4	09:55:43.95	69:40:35.49	0.35	0.38 ± 0.23	-3.41 ± 0.23	0.86 ± 0.13	-3.95 ± 0.13	338.4 ± 0.5	334.2 ± 0.3
			0.40	0.50 ± 0.22	-3.32 ± 0.21	0.54 ± 0.12	-3.86 ± 0.12	391.0 ± 0.6	387.1 ± 0.3
			0.45	0.61 ± 0.20	-3.25 ± 0.20	0.42 ± 0.12	-3.67 ± 0.12	437.8 ± 0.6	433.5 ± 0.4

Notes.
[a] Measurement of $F475W$ from epoch 1 at $t = 277$ days.
[b] Measurement of $F475W$ from epoch 2 at $t = 416$ days.

consistent with the pre-explosion configuration suggested by an SN exploding inside a planetary nebula.

4.1.2. Double-degenerate Models

Different double-degenerate models predict different time histories for the mass ejection prior to the final explosion triggered by virtue of the coalescence between the two WDs. For example: (1) the mass stripped and ejected through the "tidal tail" during the dynamics of compact WD merger (Raskin & Kasen 2013); (2) the mass outflow during the unstable final stage of rapid mass accretion immediately preceding the merger (Guillochon et al. 2010; Dan et al. 2011); (3) the outflow due to magnetorotationally driven disk wind (Ji et al. 2013); and (4) the ejection of a H-rich layer surrounding a He WD during the interaction between a He WD and a C/O WD companion (Shen et al. 2013). These four mechanisms predict different masses and locations of dust. Margutti et al. (2014) provided a thorough discussion based on the *Chandra* observation of SN 2014J. The non-detection by *Chandra* of CSM around SN 2014J implies a low-density environment with $n_{\rm CSM} < 3$ cm^{-3} at $\sim 10^{16}$ cm from the SN, assuming a wind velocity $v_{\rm ej} \sim$ a few 100 km s^{-1} (or lower) as typical velocity of the ejected material. The immediate SN environment depends on $\Delta t_{\rm ex}$, which is the time lag between the last major pre-explosion mass ejection and the SN explosion. The inferred distance of dust from the SN permits the time elapsed since this event to be estimated for an assumed ejection velocity ($v_{\rm ej}$). In the following, we discuss the predictions of the above four mechanisms inferred from the detection of $\gtrsim 5 \times 10^{-4} M_\odot$ CSM at a distance of $\sim 5.1 \times 10^{17}$ cm, together with the non-detection at a distance of $\sim 6.1 \times 10^{16}$ cm and beyond the distance of $\sim 7.7 \times 10^{17}$ cm.

(1) Tidal tail ejection. Prior to coalescence, as a major consequence of a merger of two compact WDs, a small fraction of the system mass will be expelled and leave the system at the escape velocity. A 3D hydrodynamics simulation shows that a

mass of $(1 - 5) \times 10^{-3} M_\odot$ will be lost from the system and achieve an escape velocity of $v_{\rm ej} \approx 2000$ km s^{-1} (Raskin & Kasen 2013). The ejecta are highly nonaxisymmetric and have opening angles of $\approx 93°$ and $\approx 41°$ in the plane of the disk and perpendicular to it, respectively. The estimated mass and inferred clumpy profile of the ejecta from our observations of SN 2014J both agree well with the predictions of tidal tail ejection (Raskin & Kasen 2013). However, the time lag, $\Delta t_{\rm ex}$, which determines the distance of the pre-explosion ejecta, is unclear. For $v_{\rm ej} \approx 2000$ km s^{-1}, our observations indicate that $\Delta t_{\rm ex} \approx 80$ years.

(2) Mass outflows during rapid accretion. Guillochon et al. (2010) and Dan et al. (2011) have shown that the mass transfer between a pure He WD or a He/CO hybrid and a CO WD can be unstable. Therefore, high-density regions may build up that lead to surface detonations that trigger the final thermonuclear runaway. During the rapid mass accretion process (with rates reaching $\sim 10^{-5}$–$10^{-3} M_\odot$ s^{-1} at final tens of orbits), a mass of $M_{\rm ej} \sim 10^{-2}$–$10^{-3} M_\odot$ will be lost through the system's Roche surface at $v_{\rm ej} \sim$ a few 1000 km s^{-1}. Our observations would imply that substantial material can be ejected as early as several decades before the coalescence. This is comparable to the mass limit at $\sim 10^{16}$ cm set by the *Chandra* X-ray observation (Margutti et al. 2014).

(3) Disk winds. During the WD–WD merger, an unstable, magnetorotationally driven accretion disk will be produced before the detonation leading to the explosion of a type Ia SN. Simulations suggest that about $10^{-3} M_\odot$ will become gravitationally unbound and be ejected at a mean velocity $v_{\rm ej} \sim 2600$ km s^{-1} (Ji et al. 2013). This outflow produced by magnetorotationally driven turbulence within the disk yields a time history of the mass ejection similar to that predicted by the tidal tail ejection (Raskin & Kasen 2013); our observations suggest $\Delta t_{\rm ex} \approx 60$ years. These magnetized outflows are predicted to be strongly nonaxisymmetric, with an opening
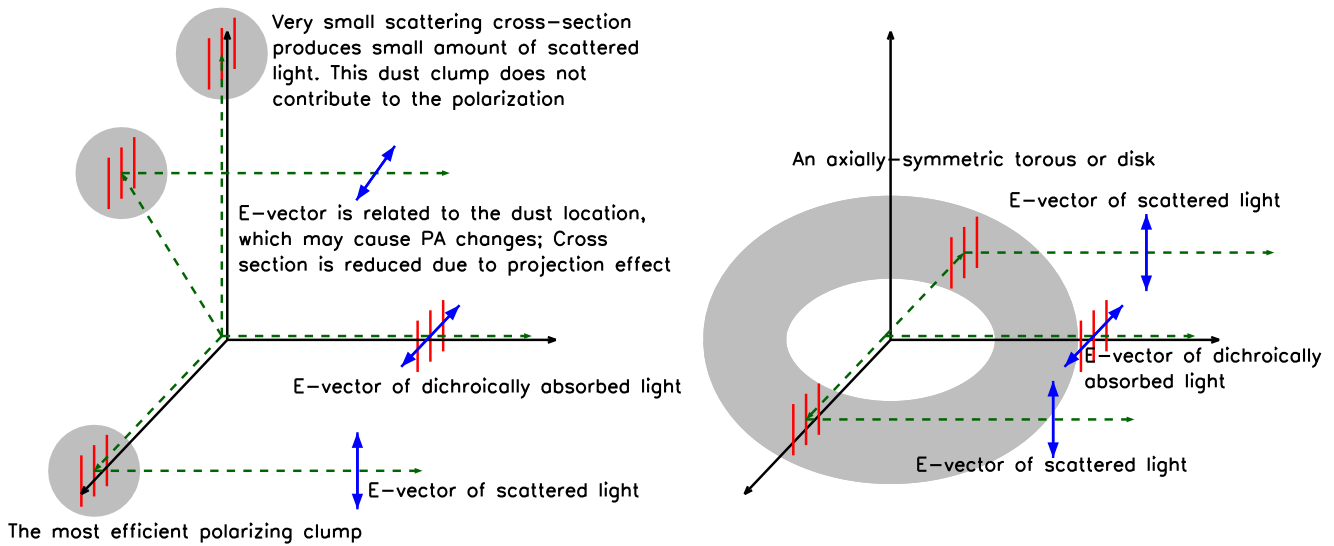
Figure 8. Schematic diagram explaining the non-local coherence of the polarization PA in the case that the grains in circumstellar dust clumps are aligned with the local interstellar magnetic field. Red bars illustrate dust grains aligned by an ad hoc coherent magnetic field, green dashed lines represent light from the SN, and blue arrows demonstrate the direction of E-vectors of the net polarized light. The observer is located outside the right edge of the figure. In the right panel, the net effect is a rotation in the QU plane through 180°; therefore, the scattered light does not impose a rotation on the PA of integrated light measured from the SN point source.

angle of ~50°. This is also consistent with the inferred clumpy structure of the circumstellar dust cloud.

(4) Shell ejection. In a system with a C/O WD accreting He from a He-burning star, an explosion in the He layer would trigger the detonation of the C/O core (Livne 1990). In this double-detonation context, Shen et al. (2013) have proposed that a H-rich layer surrounding the He core WD would impact the mass transfer and its ejection. Their simulations suggest that the H-rich material will be removed from the binary system through multiple mass ejections over the course of 200–1400 years prior to the merger. The total ejected mass is $M_{ej} = (3-6) \times 10^{-5} M_{\odot}$ and $v_{ej} \approx 1500$ km s^{-1}, roughly equal to the velocity of a He WD in a circular orbit. Our polarimetric tomography of the circumstellar environment around SN 2014J did not find significant amount of dust at distance[13] of ~8 × 10^{16} (day 33), and beyond ~(1–3) × 10^{18} cm (after day 416). The detected $\gtrsim 5 \times 10^{-4} M_{\odot}$ CSM at a distance of ~5.1 × 10^{17} cm is roughly an order of magnitude larger than the total mass predicted for shell ejection. Furthermore, $\Delta t_{ej} \approx 107$ year is less than the 200–1400 years expected from the model.

Based on the above interpretations, we conclude that the mass of the pre-explosion ejecta and the time delay between such an event and the SN explosion are broadly consistent with most of the double-degenerate models discussed in Margutti et al. (2014). While the polarimetry of SN 2014J contributes important information to our understanding of the nature and pre-explosion evolution of the progenitors of type Ia SNe, it cannot discriminate between single- and double-degenerate models. We are also unsure about whether the double-degenerate models provide the proper temperature and density on the right timescale to enable dust formation in the implied timespan, i.e., several decades to a century. This issue needs to be addressed in the future.

4.2. Polarization PA and Dust Alignment

As shown in Table 2, the degree of polarization decreased to ~3.8% on day 277 from the interstellar polarization (~4.9%), and restored to ~4.6% on day 416. However, the polarization PA at day 277 and day 416 exhibit no time evolution, except in the i-band data taken on day 416, where the degree of polarization is low and the PA suffers larger uncertainties. A possible explanation is that the dust particles in the scattering cloud(s) are nonaxisymmetric and aligned with the foreground dust that is responsible for the extinction. The magnetic field close to the SN progenitor may be highly coherent and very efficient in quickly aligning dust particles. This is qualitatively discussed in the following paragraphs.

When light from an SN is scattered by circumstellar dust grains, the E-vector will be perpendicular to the scattering plane, such that the polarization PA is related to the location of the dust—here approximated by a single clump. We also assume that the cross-section of aligned dust grains is larger along their major axis, and the polarization is strongest when the grains' major axis is perpendicular to the scattering plane. For instance, needle-like grains at a right angle to the scattering plane can produce a significant amount of polarization. If a large-scale magnetic field permeates both the circumstellar dust and the line-of-sight ISM, it may align the grains in the dust clump and in the ISM to the same direction. Consequently, the E-vector of dichroically absorbed light on the direct SN-Earth line of sight is normal to that of the light scattered by circumstellar dust. Figure 8 gives schematic views of the net E-vector generated by circumstellar scattering and dichroic extinction.

The scattered light will be polarized with the E-vector perpendicular to the scattering plane, whereas the transmitted light will have an E-vector preferably absorbed in this direction. If the dust grains in the foreground ISM and the circumstellar dust are both aligned by the same local interstellar magnetic field, this explains why the polarization decreases as the unresolved circumstellar light echo studied in this paper emerges. Most efficiently scattering (and polarizing) dust consists of particles aligned with the ambient magnetic field.

---

[13] Assuming the scattering angle of the dust cloud to be 90°.

Under this assumption, the aligned interstellar grains do not impose a rotation on the integrated polarization of the SN point source. Otherwise, the scattered light may contribute only a few percent to the total received light, so the rotation is small (i.e., barely measurable). This holds even in the more general case in which the scattering polarization in the resolved circumstellar light echoes and the direct line-of-sight interstellar polarization are not perpendicular. However, if the circumstellar light echoes are contributing more substantially to the total signal, rotation in the integrated PA with respect to the interstellar direction is expected if the polarization PA in circumstellar light echoes is not perpendicular to the local interstellar magnetic field.

This reasoning permits an independent limit to be set on the flux contribution of the light echo. The observed polarization is a vector combination of the interstellar polarization and circumstellar polarization. After correcting the instrumental polarization and projecting these two polarization components onto the Q and U axes, we can rewrite Equations (2) and (3) as follows:

$$p\% = \sqrt{(q_{\rm isp} + q_{\rm csp})^2 + (u_{\rm isp} + u_{\rm csp})^2}, \tag{21}$$

$$\mathrm{PA} = \frac{1}{2}\tan^{-1}\left(\frac{u_{\rm isp} + u_{\rm csp}}{q_{\rm isp} + q_{\rm csp}}\right), \tag{22}$$

where superscripts isp and csp correspondingly denote the interstellar and circumstellar polarization. If we assume the polarization imparted by the scattering is $\sim 50\%$, Equations (21) and (22) imply that, if the maximal change in PA is $\sim 3°$, the polarized flux contributed by a light echo to the total polarized flux observed from SN 2014J should not exceed $\sim 10\%$, and the contribution by a light echo to the total observed flux from SN 2014J should not exceed 1%. This $\sim 3°$ variation in PA is comparable to the observed $\Delta\mathrm{PA} = 2°\!.6 \pm 1°\!.0$ in $F475W$ from V1 and V2. For the most efficient case of circumstellar polarization, i.e., by a single clump of astronomical silicate with $a = 0.1\ \mu m$ at $\sim 114°$ (Section 3.2), the polarization decrease observed on day 277 (from $\sim 4.9\%$ to $\sim 3.8\%$) can be explained with a $\sim 1\%$ flux contribution from the light echoes in the $F475W$-band, as is also illustrated by the inset panel in Figure 3. Therefore, based on the deviant integrated degree of polarization and the invariant PA observed on day 277, we infer that the rotation of the PA introduced by the circumstellar light echoes around SN 2014J is less than $\sim 3°$ with respect to the interstellar polarization. This number is model-dependent, but the most efficient configuration for producing polarized light is that in which the circumstellar dust grains are aligned with the ambient interstellar magnetic field. In this scheme, we discuss some other implications as follows.

Circumstellar dust composed of needle-like grains aligned with the interstellar magnetic field has a net polarizing effect even if its spatial distribution is spherically symmetric. The reason is that scattering in planes aligned with the grains would produce zero polarization. Therefore, it would not lead to a cancellation of the polarization produced by scattering on planes perpendicular to the dust alignment, and a net polarization arises (as illustrated by Figure 4). This indicates

that the polarization of light echoes is not necessarily an indication of the nonaxisymmetry of the dust distribution.

Polarization traces the magnetic field and enables a unique approach to the study of its interaction with nonaxisymmetric dust. Careful studies of dust grains aligned through the "radiative alignment torque" (RAT) are able to provide testable predictions on various properties (Lazarian & Hoang 2007). Andersson & Potter (2010) found that dust surrounding the Herbig Ae/Be star HD 97300 does not align with the stellar wind, ruling out significant contributions to grain alignment through the stellar wind or radiation pressure of the star (the so-called Gold alignment; see, e.g., Gold 1952). At a star-cloud distance of $\sim 0.03\ \mathrm{pc}$, a weak dependence of the grain-alignment efficiency on the angle between the magnetic field and the radiation field anisotropy is seen (Andersson & Potter 2010). This confirms the grain alignment predicted by the RAT model. Furthermore, dust grains in the vicinity of a type Ia SN may be more efficiently aligned by the radiative torque of the SN radiation. Among all the single- and double-degenerate cases with time lags around decades to a century, the growth in grain size of the pre-explosion ejecta may not be particularly relevant, considering the relatively long timescale of the grain growth; see Figure 8 of Mattsson (2016). These small grains can be effectively aligned by the SN radiation regardless of the relatively small effect of the interstellar radiation field. For instance, at distances of 1–10 pc, $a \sim 0.03\ \mu m$ grains can be radiatively aligned within ~ 0.5–40 days for SN luminosity of $10^8\ L_\odot$ (Hoang 2017). However, lacking further observational constraints, we conclude that it remains unclear whether an intrinsic magnetic field of the progenitor of SN 2014J or the ambient magnetic field in the ISM of M82 could align the dust grains quickly enough within the relatively short time (estimated above at ~ 160 years) between the pre-explosion mass ejection and the SN explosion.

It is also possible that the dust grains in the pre-explosion ejecta are aligned neither with a magnetic field nor the radiation torque of the SN radiation, i.e., exhibit no dominant directional preference. Instead of being elongated but randomly oriented, dust grains may alternatively have nearly spherical shape with little polarizing power because the difference between minimal and maximal extinction efficiencies is small. In all these cases, the deviant integrated degree of polarization and the invariant PA observed on day 277 require the dust to be at certain PA relative to the SN, i.e., the scattering plane is perpendicular to the interstellar magnetic field. This would introduce an orthogonal polarization component to the integrated light. Under these circumstances, the vectorial combination of the two components only affects the degree of polarization, but not the PA, as observed in SN 2014J.

It is important to stress that resolved light echoes around SN 2014J caused by interstellar dust (Crotts 2015; Yang et al. 2017) do not compromise the inference of circumstellar dust from the evolution of non-spatially resolved polarization. The scattering angle by foreground ISM is $\theta \sim \sqrt{2ct/z} \sim 4°\!.5\left(\frac{t}{1\ \mathrm{year}}\frac{100\ \mathrm{pc}}{z}\right)^{1/2}$, where t denotes the time after optical maximum and z is the foreground distance of the dust to the SN. At such small scattering angles, the polarization of resolved light echoes results from the dichroic extinction by partially aligned non-spherical paramagnetic dust grains. This interstellar polarization can be determined from the SN polarization around maximum light (Kawabata et al. 2014; Patat et al. 2015). Moreover, any such polarization signal that,

at the distance of M82, is unresolved by *HST* is expected to be constant with time. Therefore, it cannot explain the deviant measurement on day 277.

One other possibility is that SN 2014J exploded close to some pre-existing interstellar dust clouds. The morphological evolution of the "luminous arc" light echo probed by the iso-delay light surface at day 277 and day 416 reveals the inhomogeneity of the foreground ISM that transformed from three clumps to two short segments of concentric arcs (see Figure 4 of Yang et al. 2017). This implies that the ISM in the vicinity of the SN 2014J-Earth line of sight is inhomogeneous on scales smaller than $\sim$2.3 pc at a foreground distance of 226 pc (see the projected radius at day 277 and day 416 in Table 4 of Yang et al. 2017). This does not invalidate the claims of the small R_V variations of Galactic dust in a local kilo-parsec volume probed with a spatial resolution of $\sim$60 pc and within only $\sim$100 pc scale height ($R_V = 3.0 \pm 0.2$, Schlafly et al. 2017). Recently, based on low-resolution spectro-polarimetric observations of multiple sight-lines, Sie-benmorgen et al. (2017) found significant variations of the Galactic dust characteristics on small scales, as well as from cloud to cloud (i.e., $2.3 \leqslant R_V \leqslant 5.0$). Smaller scales of inhomogeneity of the ISM in M82 may still be possible. Therefore, we cannot rule out the possibility that the scattering dust cloud(s) producing the late-time deviation in polarimetry of SN 2014J is part of the ISM close to SN 2014J.

5. Summary

Monitoring with the imaging polarimetry mode of the *HST* ACS/WFC, at six epochs from 277 and 1181 days after the maximum light, has probed the circumstellar environment of the type Ia supernova 2014J. On day 277, the polarization exhibited a conspicuous deviation from all other epochs. This difference can result from light scattered by circumstellar ejecta of $\gtrsim 5 \times 10^{-4} M_\odot$ located $\sim 5 \times 10^{17}$ cm ($\sim$0.5 light years) from SN 2014J. The polarization at other epochs is consistent with the interstellar polarization around the optical maximum. This rules out significant circumstellar dust at distances between $\sim$1 and $\sim$3.3 light years from SN 2014J. If attributed to the progenitor of SN 2014J, the distance of the dust from the SN constrains the time of ejection. It is consistent with a single-degenerate model with an unsteady mass loss, i.e., experiencing a nova-like eruption about 160 years before the SN explosion for a typical speed of 1000 km s^{-1}. The inferred mass and distance of the circumstellar dust cloud are also consistent with an explosion inside a planetary nebula including dense clumps.

In most of the double-degenerate models, a significant amount of mass ($\sim 10^{-4} - 10^{-2} M_\odot$) will be ejected prior to the coalescence between the two WDs. The time lag between the pre-explosion mass ejection and the final explosion ranges from hundreds of seconds to about a century, depending on the model we have discussed in Section 4.1.2. The mass-loss history deduced from the late-time polarimetry of SN 2014J is consistent with most of the double-degenerate scenarios discussed in Margutti et al. (2014) and references therein. Despite providing important constraints on the nature and pre-explosion evolution of the progenitors of type Ia SNe, our time-resolved precision polarimetry with *HST* could not discriminate between single- and double-degenerate models.

The single-event-like time dependence of the degree of the polarization and the constancy of the polarization angle can be unde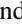rstood if the circumstellar du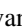st of SN 2014J is aligned with the ambient interstellar magnetic field. However, both grains with low asymmetry and elongated grains aligned by the radiative torque by the progenitor's radiation could lead to the same effect if the dust cloud is located at an angle of $\sim$90° to the PA of the ambient interstellar polarization. Polarimetry of light echoes around Galactic novae can enable critical tests of the alignment mechanism of dust grains.

We have presented a novel method for probing the circumstellar environment of type Ia SN. This method uses the time evolution of SN polarization at late epochs to constrain the mass and distance of material inhomogeneously distributed around the SN. When a significant time evolution of polarization is observed at a location close to the SN, as implied by the elapsed time and the angular separation, we will be able to place stringent constraints on the presence of circumstellar dust. Although our current data cannot place solid criteria to distinguish between the single- and double-degenerate channels for type Ia SNe explosion, polarimetry at late times may emerge as a new and effective way of systematically studying the progenitor systems of type Ia SNe. Future observations of the type Ia SNe at late epochs will help to address the nature of circumstellar dust around type Ia SNe and their effect on the reddening and extinction toward the SNe.

ORCID iDs

Yi Yang (杨轶) ⓘ https://orcid.org/0000-0002-6535-8500
Peter. J. Brown ⓘ https://orcid.org/0000-0001-6272-5507
Aleksandar Cikota ⓘ https://orcid.org/0000-0001-7101-9831

Misty Cracraft ⬥ https://orcid.org/0000-0002-7698-3002
Justyn R. Maund ⬥ https://orcid.org/0000-0003-0733-7215
Ferdinando Patat ⬥ https://orcid.org/0000-0002-0537-3573
William B. Sparks ⬥ https://orcid.org/0000-0002-9011-6829
Jason Spyromilio ⬥ https://orcid.org/0000-0001-6815-4055
Heloise F. Stevance ⬥ https://orcid.org/0000-0002-0504-4323
Xiaofeng Wang ⬥ https://orcid.org/0000-0002-7334-2357
J. Craig Wheeler ⬥ https://orcid.org/0000-0003-1349-6538

References

Amanullah, R., & Goobar, A. 2011, ApJ, 735, 20
Amanullah, R., Goobar, A., Johansson, J., et al. 2014, ApJL, 788, L21
Andersson, B.-G., & Potter, S. B. 2010, ApJ, 720, 1045
Avila, R. 2017, ACS Instrument Handbook, Version 16.0 (Baltimore, MD: STScI)
Barbon, R., Ciatti, F., & Rosino, L. 1973, A&A, 25, 241
Biretta, J., Kozhurina-Platais, V., Boffi, F., Sparks, W., & Walsh, J. 2004, ACS Polarization Calibration—I. Introduction and Status Report ACS 2004-09, Tech. Rep. (Baltimore, MD: STScI)
Bloom, J. S., Kasen, D., Shen, K. J., et al. 2012, ApJL, 744, L17
Bonanos, A. Z., & Boumis, P. 2016, A&A, 585, A19
Brown, P. J., Smitka, M. T., Wang, L., et al. 2015, ApJ, 805, 74
Bulla, M., Goobar, A., Amanullah, R., Feindt, U., & Ferretti, R. 2018, MNRAS, 473, 1918
Bulla, M., Sim, S. A., Pakmor, R., et al. 2016, MNRAS, 455, 1060
Cao, Y., Kulkarni, S. R., Howell, D. A., et al. 2015, Natur, 521, 328
Cardelli, J. A., Clayton, G. C., & Mathis, J. S. 1989, ApJ, 345, 245
Chevalier, R. A. 1986, ApJ, 308, 225
Cikota, A., Deustua, S., & Marleau, F. 2016, ApJ, 819, 152
Cracraft, M., & Sparks, W. B. 2007, ACS Polarization Calibration—Data, Throughput, and Multidrizzle Weighting Schemes, Instrument Science Report ACS 2007-10, Tech. Rep. (Baltimore, MD: STScI)
Crotts, A. P. S. 2015, ApJL, 804, L37
Dalcanton, J. J., Williams, B. F., Seth, A. C., et al. 2009, ApJS, 183, 67
Dan, M., Rosswog, S., Guillochon, J., & Ramirez-Ruiz, E. 2011, ApJ, 737, 89
Draine, B. T. 2003, ApJ, 598, 1017
Draine, B. T., & Lee, H. M. 1984, ApJ, 285, 89
Elias, J. H., Frogel, J. A., Hackwell, J. A., & Persson, S. E. 1981, ApJL, 251, L13
Fitzpatrick, E. L. 1999, PASP, 111, 63
Foley, R. J., Fox, O. D., McCully, C., et al. 2014, MNRAS, 443, 2887
Fossey, J., Cooke, B., Pollack, G., Wilde, M., & Wright, T. 2014, CBET, 3792, 1
Gold, T. 1952, MNRAS, 112, 215
Gonzaga, S., Hack, W., Fruchter, A., & Mack, J. 2012, The DrizzlePac Handbook (Baltimore, MD: STScI)
González Hernández, J. I., Ruiz-Lapuente, P., Tabernero, H. M., et al. 2012, Natur, 489, 533
Goobar, A. 2008, ApJL, 686, L103
Goobar, A., Kromer, M., Siverd, R., et al. 2015, ApJ, 799, 106
Graham, M. L., Valenti, S., Fulton, B. J., et al. 2015, ApJ, 801, 136
Greenberg, J. M. 1986, Natur, 321, 385
Guillochon, J., Dan, M., Ramirez-Ruiz, E., & Rosswog, S. 2010, ApJL, 709, L64
Henyey, L. G., & Greenstein, J. L. 1941, ApJ, 93, 70
Hoang, T. 2017, ApJ, 836, 13
Hosseinzadeh, G., Sand, D. J., Valenti, S., et al. 2017, ApJL, 845, L11
Hoyle, F., & Fowler, W. A. 1960, ApJ, 132, 565
Iben, I., Jr. 1982, ApJ, 259, 244
Iben, I., Jr., & Tutukov, A. V. 1984, ApJS, 54, 335
Ji, S., Fisher, R. T., García-Berro, E., et al. 2013, ApJ, 773, 136
Johansson, J., Goobar, A., Kasliwal, M. M., et al. 2017, MNRAS, 466, 3442
Kaneda, H., Ishihara, D., Suzuki, T., et al. 2010, A&A, 514, A14
Kasen, D. 2010, ApJ, 708, 1025
Kawabata, K. S., Akitaya, H., Yamanaka, M., et al. 2014, ApJL, 795, L4
Kawabata, K. S., Nagae, O., Chiyonobu, S., et al. 2008, Proc. SPIE, 7014, 70144L
Kelly, P. L., Fox, O. D., Filippenko, A. V., et al. 2014, ApJ, 790, 3
Kervella, P., Bond, H. E., Cracraft, M., et al. 2014, A&A, 572, A7
Kerzendorf, W. E., Childress, M., Scharwächter, J., Do, T., & Schmidt, B. P. 2014, ApJ, 782, 27
Kerzendorf, W. E., Strampelli, G., Shen, K. J., et al. 2017, MNRAS, submitted (arXiv:1709.06566)

Kundu, E., Lundqvist, P., Pérez-Torres, M. A., Herrero-Illana, R., & Alberdi, A. 2017, ApJ, 842, 17
Laor, A., & Draine, B. T. 1993, ApJ, 402, 441
Lazarian, A., & Hoang, T. 2007, MNRAS, 378, 910
Li, W., Bloom, J. S., Podsiadlowski, P., et al. 2011, Natur, 480, 348
Livio, M., & Truran, J. W. 1992, ApJ, 389, 695
Livne, E. 1990, ApJL, 354, L53
Lucas, R., et al. 2016, ACS Data Handbook, Version 8.0 (Baltimore, MD: STScI), http://www.stsci.edu/hst/acs/documents/handbooks/currentDHB/
Lundqvist, P., Nyholm, A., Taddia, F., et al. 2015, A&A, 577, A39
Ma, B., Wei, P., Shang, Z., Wang, L., & Wang, X. 2014, ATel, 5794
Mann, I., Köhler, M., Kimura, H., Cechowski, A., & Minato, T. 2006, A&ARv, 13, 159
Margutti, R., Parrent, J., Kamble, A., et al. 2014, ApJ, 790, 52
Marion, G. H., Brown, P. J., Vinkó, J., et al. 2016, ApJ, 820, 92
Mathis, J. S., & Whiffen, G. 1989, ApJ, 341, 808
Mattsson, L. 2016, P&SS, 133, 107
Maund, J. R., Spyromilio, J., Höflich, P. A., et al. 2013, MNRAS, 433, L20
Mie, G. 1908, AnP, 330, 377
Montier, L., Plaszczynski, S., Levrier, F., et al. 2015, A&A, 574, A135
Nobili, S., & Goobar, A. 2008, A&A, 487, 19
Noguchi, T., Ohashi, N., Tsujimoto, S., et al. 2015, E&PSL, 410, 1
Nugent, P. E., Sullivan, M., Cenko, S. B., et al. 2011, Natur, 480, 344
Olling, R. P., Mushotzky, R., Shaya, E. J., et al. 2015, Natur, 521, 332
Patat, F. 2005, MNRAS, 357, 1161
Patat, F., Benetti, S., Cappellaro, E., & Turatto, M. 2006, MNRAS, 369, 1949
Patat, F., Chandra, P., Chevalier, R., et al. 2007, Sci, 317, 924
Patat, F., & Taubenberger, S. 2011, A&A, 529, A57
Patat, F., Taubenberger, S., Cox, N. L. J., et al. 2015, A&A, 577, A53
Pérez-Torres, M. A., Lundqvist, P., Beswick, R. J., et al. 2014, ApJ, 792, 38
Perlmutter, S., Aldering, G., Goldhaber, G., et al. 1999, ApJ, 517, 565
Petrova, E. V., Jockers, K., & Kiselev, N. N. 2000, Icar, 148, 526
Phillips, M. M. 1993, ApJL, 413, L105
Porter, A. L., Leising, M. D., Williams, G. G., et al. 2016, ApJ, 828, 24
Raskin, C., & Kasen, D. 2013, ApJ, 772, 1
Riess, A. G., Filippenko, A. V., Challis, P., et al. 1998, AJ, 116, 1009
Riess, A. G., Macri, L. M., Hoffmann, S. L., et al. 2016, ApJ, 826, 56
Rimoldi, A., Portegies Zwart, S., & Rossi, E. M. 2016, ComAC, 3, 2
Ruiz-Lapuente, P., Comeron, F., Méndez, J., et al. 2004, Natur, 431, 1069
Sand, D. J., Hsiao, E. Y., Banerjee, D. P. K., et al. 2016, ApJL, 822, L16
Schaefer, B. E., & Pagnotta, A. 2012, Natur, 481, 164
Schlafly, E. F., Peek, J. E. G., Finkbeiner, D. P., & Green, G. M. 2017, ApJ, 838, 36
Schulz, R., Hilchenbach, M., Langevin, Y., et al. 2015, Natur, 518, 216
Sen, A., Botet, R., Vilaplana, R., Choudhury, N. R., & Gupta, R. 2017, JQSRT, 198, 164
Serkowski, K. 1958, AcA, 8, 135
Serkowski, K. 1962, AdA&A, 1, 289
Serkowski, K., Mathewson, D. S., & Ford, V. L. 1975, ApJ, 196, 261
Shen, K. J., Guillochon, J., & Foley, R. J. 2013, ApJL, 770, L35
Siebenmorgen, R., Voshchinnikov, N. V., Bagnulo, S., et al. 2017, A&A, in press (arXiv:1711.08672)
Sirianni, M., Jee, M. J., Benítez, N., et al. 2005, PASP, 117, 1049
Sparks, W. B. 1994, ApJ, 433, 19
Sparks, W. B., & Axon, D. J. 1999, PASP, 111, 1298
Sparks, W. B., Bond, H. E., Cracraft, M., et al. 2008, AJ, 135, 605
Srivastav, S., Ninan, J. P., Kumar, B., et al. 2016, MNRAS, 457, 1000
Starrfield, S., Sparks, W. M., & Truran, J. W. 1985, ApJ, 291, 136
Sugerman, B. E. K. 2003, AJ, 126, 1939
Tsebrenko, D., & Soker, N. 2013, MNRAS, 435, 320
Tsebrenko, D., & Soker, N. 2015, MNRAS, 450, 1399
Tylenda, R. 2004, A&A, 414, 223
Volten, H., Muñoz, O., Hovenier, J. W., et al. 2007, A&A, 470, 377
Voshchinnikov, N. V., Henning, T., Prokopjeva, M. S., & Das, H. K. 2012, A&A, 541, A52
Wang, L. 2005, ApJL, 635, L33
Wang, L., Baade, D., Höflich, P., et al. 2004, ApJL, 604, L53
Wang, L., & Wheeler, J. C. 1996, ApJL, 462, L27
Wang, L., Wheeler, J. C., Wang, L., & Wheeler, J. C. 2008, ARA&A, 46, 433
Webbink, R. F. 1984, ApJ, 277, 355
Weingartner, J. C., & Draine, B. T. 2001, ApJ, 548, 296
Wheeler, J. C. 2012, ApJ, 758, 123
Wood-Vasey, W. M., & Sokoloski, J. L. 2006, ApJL, 645, L53
Yang, Y., Wang, L., Baade, D., et al. 2017, ApJ, 834, 60
Yang, Y., Wang, L., Baade, D., et al. 2018, ApJ, 852, 89
Yaron, O., Prialnik, D., Shara, M. M., & Kovetz, A. 2005, ApJ, 623, 398
Zheng, W., Shivvers, I., Filippenko, A. V., et al. 2014, ApJL, 783, L24